

Photometric Redshift of X-Ray Sources in the Chandra Deep Field South¹

W. Zheng², V. J. Mikles,^{2,3}, V. Mainieri^{4,5}, G. Hasinger⁵, P. Rosati⁴, C. Wolf⁶,
C. Norman^{2,7}, G. Szokoly⁵, R. Gilli⁸, P. Tozzi⁹, J. X. Wang², A. Zirm¹⁰, and R. Giacconi^{11,2}

ABSTRACT

Based on the photometry of 10 near-UV, optical, and near-infrared bands of the Chandra Deep Field South, we estimate the photometric redshifts for 342 X-ray sources, which constitute $\sim 99\%$ of all the detected X-ray sources in the field. The models of spectral energy distribution are based on galaxies and a combination of power-law continuum and emission lines. Color information is useful for source classifications: Type-I AGN show non-thermal spectral features that are distinctive from galaxies and Type-II AGN. The hardness ratio in X-ray and the X-ray-to-optical flux ratio are also useful discriminators. Using rudimentary color separation techniques, we are able to further refine our photometric redshift estimations. Among these sources, 137 have reliable spectroscopic redshifts, which we use to verify the accuracy of photometric redshifts and to modify the

¹Based on observations performed at the European Southern Observatory and observations with the NASA/ESA Hubble Space Telescope, obtained at the Space Telescope Science Institute, which is operated by the Association of Universities of Research in Astronomy, Inc., under NASA contract NAS5-26555

²Center for Astrophysical Sciences, Department of Physics and Astronomy, The Johns Hopkins University, Baltimore, MD 21218-2686, USA

³Department of Astronomy, University of Florida, Gainesville, FL 32611, USA

⁴European Southern Observatory, Karl-Schwarzschild-Strasse 2, D-85748 Garching, Germany

⁵Max-Plank-Institut für Extraterrestrische Physik, Giessenbachstrasse Postfach 1312, D-85741 Garching, Germany

⁶Department of Physics, Denys Wilkinson Building, University of Oxford, Keble Road, Oxford, OX1 3RH, United Kingdom

⁷Space Telescope Science Institute, 3700 San Martin Drive, Baltimore, MD 21218, USA

⁸Osservatorio Astrofisico di Arcetri, Largo E. Fermi 5, 50125 Firenze, Italy

⁹Osservatorio Astronomico di Trieste, via G. Tiepolo 11, 34131 Trieste, Italy

¹⁰Department of Astronomy, Leiden Observatory, P. O. Box 9513, 2300 RA, Leiden, The Netherlands

¹¹Associated Universities Inc., 1400 16th Street NW, Washington DC 20036, USA

model inputs. The average relative dispersion in redshift distribution is $\sim 8\%$, among the most accurate for photometric surveys. The high reliability of our results is attributable to the high quality and broad coverage of data as well as the applications of several independent methods and a careful evaluation of every source. We apply our redshift estimations to study the effect of redshift on broadband colors and to study the redshift distribution of AGN. Our results show that both the hardness ratio and U-K color decline with redshift, which may be the result of a K-correction. The number of Type-II AGN declines significantly at $z > 2$ and that of galaxies declines at $z > 1$. However, the distribution of Type-I AGN exhibits less redshift dependence. As well, we observe a significant peak in the redshift distribution at $z=0.6$. We demonstrate that our photometric redshift estimation produces a reliable database for the study of X-ray luminosity of galaxies and AGN.

Subject headings: galaxies: active — galaxies: distances and redshifts — galaxies: photometry — X-rays: galaxies — X-rays: general

1. INTRODUCTION

The Chandra Deep Field South (CDFS, Giacconi et al. 2000; Tozzi et al. 2001; Rosati et al. 2002; Giacconi et al. 2002), with approximately one million seconds of accumulated exposure, reaches a limiting flux of 5.5×10^{-17} ergs s $^{-1}$ cm $^{-2}$ in the 0.5-2 keV band and 4.5×10^{-16} ergs s $^{-1}$ cm $^{-2}$ in the 2-10 keV band. This is more than 20 times deeper than the *ROSAT* deep survey (Hasinger et al. 1998). Within a $17' \times 17'$ field, 346 X-ray sources are identified. CDFS has become one of best-studied fields in the sky, and its importance increases significantly with the GOODS observations (Dickinson et al. 2003) and the Hubble Ultra Deep Field (UDF, Beckwith et al. 2003).

To reveal the nature and properties of these faint X-ray sources, extensive follow-up observations have been made in many wavelength bands. Spectroscopic observations with the VLT and the FORS instrument (Szokoly et al. 2004) have yielded 168 spectra, of which 137 have reliable redshifts. In the mean time, deep imaging observations have been made with the ESO VLT and NTT in eight bands: U,B,V,R,I,J,H and K $_s$ (Renzini et al. 2003). The HST images taken by the GOODS team provide high-quality photometry and source morphology. These observations reach significantly deeper than the spectroscopic observations, therefore yield an essential multi-band database for deriving reliable photometric redshifts for the X-ray sources. They also provide two additional bands: the ACS/F850LP (z-band) and WFPC2/F300W (near-UV band).

While X-ray sources account for only a small fraction of the field galaxies, they form a special group with distinct properties. The *ROSAT* Ultra Deep Survey (Lehmann et al. 2001) indicates that the majority of X-ray sources are active galactic nuclei (AGN). Type-I AGN are characterized with broad emission lines and an underlying power-law continuum, and the Type-II AGN exhibit prominent narrow emission lines. The combined results of CDFS and Chandra Deep Field North (Gilli et al. 2003b) further confirm that they are consistent with an assumption that obscured AGN (Type-II) outnumber normal, unobscured (Type-I) AGN by a factor of approximately 4-10.

A key parameter of these extremely faint X-ray sources is their redshifts, which may be determined spectroscopically or photometrically. The spectral-energy-distribution (SED) method of redshift estimation (photometric redshift, Koo 1985; Connolly et al. 1997; Bolzonella et al. 2000; Benítez 2000) uses a library of SED templates of galaxies at varying redshifts to fit the observed broadband data with a minimization of χ^2 . The most prominent feature in these templates is a Balmer break around 4000 Å in the rest frame, because of the thermal nature of the galaxy continuum. At high redshift ($z \gtrsim 2$), intergalactic absorption shortward of Ly α produces a significant break at 1216 $(1+z)$ Å. These breaks or other strong spectral features can leave a distinctive signature across the range of passbands, making it possible to determine reasonable redshift estimates. Simulations and observations have demonstrated that photometric redshifts can be accurate on the order of 10% for most sources. The Sloan Digital Sky Survey (SDSS) uses five-band color selection to find quasars, galaxies and other sources (Richards et al. 2001; Budavári 2001). Photometric redshift estimation is an extension of such color selection techniques, and it has gained popularity in recent years as deep imaging surveys become one of the most important methods in probing the early universe (Arnouts et al. 2001; Wolf et al. 2001b). The majority of sources in these fields are so faint that it is impractical to obtain their spectra in large number. Redshift information used in conjunction with the optical, UV, IR, and X-ray photometry is central in determining the nature of faint X-ray sources and how they are linked to the galaxy population at similar redshift. Also, we can explore how the luminosity function of X-ray galaxies differs from that of other galaxies. A number of studies have been carried out to compare photometric and spectroscopic redshifts (Gonzalez and Maccarone 2002; Mobasher et al. 2004; Gandhi et al. 2004) for X-ray sources. A study of similar scope (Barger et al. 2003) finds that the photometric redshifts are within 25% of the spectroscopic redshifts for 94% of the non-broad-line sources with both photometric and spectroscopic measurements.

In this paper, we focus on refining our photometric redshift techniques on an X-ray selected sample of sources and testing our results against current model predictions. Our redshift estimates are based on public imaging data in the near-UV (NUV, 3000Å), optical and infrared bands. The results will facilitate our understanding of the broadband properties,

luminosity function of X-ray sources and many other important issues such as clustering and the large-scale structure of the early universe.

We discuss the data resources and processing in §2. In §3 we discuss the application of several methods of photometric redshift and compare their results to derive the most probable redshifts. With the photometric redshifts for all CDFS sources, we discuss in §4 the redshift dependence of source properties and potential implications.

2. DATA

2.1. X-Ray Data

Our sample is the 346 X-ray sources identified from the 940 ksec of CDFS data (Giacconi et al. 2002). Throughout this paper we use AB magnitudes, and we calculate the X-ray magnitudes as $X = -2.5 \log f + 2.5 \log \nu - 48.6$, where f is flux in units of $\text{ergs s}^{-1} \text{cm}^{-2}$, and $\nu = 2.4 \times 10^{17}$ and 9.5×10^{17} Hz for the soft X-ray band (0.5-2 keV) and hard X-ray band (2-10 keV), respectively. For sources not detected in one of the X-ray bands, we derive the upper limits to X-ray magnitudes. In this calculation, we consider the limiting magnitude for the soft and hard-X-ray as ~ 35.5 ($f \sim 5.5 \times 10^{-17} \text{ ergs s}^{-1} \text{cm}^{-2}$) and ~ 34.7 ($4.5 \times 10^{-16} \text{ ergs s}^{-1} \text{cm}^{-2}$), respectively. Approximately 85% of these X-ray sources have been identified in the optical R-band images of ESO VLT/FORS (Giacconi et al. 2002).

2.2. Imaging Data

The ESO/FORS R-band images cover most of the CDFS field to a limiting magnitude of ~ 26.5 . Supplementary positions are added from the comparison with the ESO Imaging Survey (EIS, Arnouts et al. 2001). The EIS images and catalogues also provide multiband information. Only objects that fall with $5''$ from the X-ray positions are selected. Each entry in the catalogs is compared with the X-ray positions (Giacconi et al. 2002). The 5σ limiting magnitudes of the EIS data are $U=25.7$, $B=26.4$, $V=25.4$, $R=25.5$, $I=24.7$, $J=23.4$, and $K_s = 22.6$. The VLT/GOODS imaging data in J , H , and K_s bands reach limiting magnitudes of ~ 25.5 .

Uncertainties of the optical zero point are in the range of 0.03 - 0.08. As our comparison of the measurements from different data indicates, real uncertainties may be larger than tabulated values. We therefore assign uniform errors of 0.1 magnitudes for most data points unless the tabulated errors are larger than 0.1. As shown in Figure 1 and Table 1, the

majority of the optical counterparts lie with $2''$ from the X-ray position, (and within $1''$ from the optical position given in Giacconi et al. (2002)).

Additional data are obtained from the COMBO-17 survey (Wolf et al. 2001a, 2003, 2004) in its most sensitive broad bands and from the GOODS images. The COMBO-17 data of the CDFS consist of catalogs in three broad bands (B, V and R), with limiting magnitudes of ~ 26 . The photometric redshift of 272 matched X-ray sources are available. In COMBO-17 every object is either classified as a star, a galaxy or a quasar, and in the latter two cases redshifts are determined. COMBO-17, because its significantly higher number of bands, provides more reliable redshift estimations, particularly for those with emission lines. A comparison between the COMBO-17 results and spectroscopic redshift yields an average error of $1 - 2\%$ (Wolf et al. 2004), better than that of our broad-band results ($\sim 8\%$). However, its advantage is limited to relatively bright sources ($R < 24$) and redshift below 1.5 or above 2.5.

The optical GOODS data (Giavalisco et al. 2004) are taken with the Advanced Camera for Surveys (ACS) on board of *HST* and filters F435W, F606W, F775W, and F850LP (B,V,I, and Z band, respectively). These data reach magnitudes of ~ 28 , therefore providing additional significant resources. The processed ACS data images and catalogs, including the UDF, are retrieved from the Multimission Archive at the Space Telescope Science Institute (MAST). We use the *SExtractor* algorithm (Bertin and Arnouts 1996) to identify sources. Since the HST data have significantly higher spatial resolution, we sum all the source fluxes within $0.^5$ from the optical positions in the EIS data, in order to match its photometry. Additional source positions are obtained for those that are not detected in either the EIS or FORS-R data. In total, data of 69 sources are added to the EIS database.

To obtain reliable colors for our sources the spread in seeing conditions for images in different wavebands has to be taken into account. We have computed corrected magnitudes according to the following strategy: 1) We computed magnitudes in apertures of $2''$ in each waveband using the available images ("original" images); 2) We degraded the point spread function (PSF) of each image to match the worst condition ("degraded" images); 3) We recomputed the magnitudes in apertures of $2''$ using the "degraded" images; and 4) We derived corrections for the different seeing conditions comparing, for stellar "bright" objects, magnitudes in the original and in the "degraded" images and applied these corrections to the "original" magnitudes.

The GOODS data also include the band of WFPC2 F300W, which provides clues that complement the optical data. In the low-redshift range, these data enable the separation of power-law continua from thermal components. At $z > 1.5$, the data may reveal the signature of prominent Ly α emission. We obtain the processed images from MAST and use IRAF tasks

to reject cosmic ray events and stack the images. A total of 112 stacked field images are produced, and each of them contains at least three independent WFPC2 images. We use *SExtractor* to identify sources from the stacked images. The limiting magnitude in this band varies with the number of stacked images. The average 5σ limiting magnitude is ~ 26 . 105 sources have detection in the NUV band, and 123 are confirmed with no detection.

In all, 191 sources have data in all ten bands: NUV, U, B, V, R, I, Z, J, H, and K_s . 326 sources have data in seven or more broad bands between U and K_s , 15 other sources have five or six bands of data. 14 sources have no infrared data. There are four objects which do not have detections in addition to the FORS-R results (Giacconi et al. 2002).

2.3. Spectroscopic Data

Spectroscopic observations of selected X-ray sources were carried out in 2000 and 2001, with the VLT telescope and FORS instrument. Details of the observations and data reduction may be found in Szokoly et al. (2004). The spectroscopic redshifts for 137 objects provide a critical source for our verifications, and the data also allow us to distinguish between broad-line and narrow-line objects. Because of the low spectroscopic resolution ($R \sim 300$), the classification of sources is tentative. As defined in Szokoly et al. (2004), objects with emission lines of $> 2000 \text{ km s}^{-1}$ are considered as Type-I AGN. Such a definition based on the opticaal spectroscopy is largely consistent with the classification by X-ray data (see §3.2 and Fig. 3), but a few exceptions do exist. Approximately twenty spectroscopic redshifts are derived from the sources fainter than the nominal limiting magnitudes of $R \sim 24$. These values are considered reliable because of the sources' prominent emission-line features.

3. MODELING

3.1. Photo-z Codes and Galaxy Templates

We calculate photometric redshifts using two parallel models: HyperZ (Bolzonella et al. 2000) and the Bayesian Model (BPZ, Benítez 2000). The results are dependent on the selection of model templates. Using spectroscopic redshifts to check the reliability of the derived photometric redshifts, we are able to choose the galaxy templates that best suit. For HyperZ, our sample of X-ray sources include starburst galaxies, E, S0, Sbc, Scd, and Im galaxies from Coleman et al. (1980) and the GISSEL98 library (Bruzual and Charlot 1993). The BPZ model combines the χ^2 minimization and Bayesian marginalization, using relevant knowledge, such as the expected shape of the redshift distributions and the galaxy type

fractions. We use the default library in the BPZ, which is similar to HyperZ but includes additional templates of starburst galaxies, and a set of flat spectra.

Both the HyperZ and BPZ models provide accurate fits for approximately 85% of the objects, however, there are a number of objects whose fitted redshifts are different from the known spectroscopic values. Most of these sources are Type-I AGN, which are known for their power-law spectra with prominent broad emission lines. Failure to detect strong broad lines in the passbands is the most likely cause for poor fits. Even in the broadband data, their difference may be significant. In Figure 2 we plot three representative sets of broadband data, plus the SDSS composite spectrum as a representation of Type-I AGN and quasars (Vanden Berk et al. 2001).

Between approximately 1200 and 5000 Å the underlying continuum may be described by a single power law. However, the SDSS composite spectrum itself does not fit all the Type-I AGN. Some Type-I AGN show relatively weak emission lines, and their continuum is dominated by a thermal continuum of the underlying galaxy, instead of a power law. We therefore generate a set of AGN spectra by combining a continuum component and emission-line components. The continuum is a broken power law. We assume a power law of $f_\nu \propto \nu^{-\alpha}$, with α varying between 0 and 1. Longward of 5000 Å we add another power-law component of $\alpha = 1.4$ to represent the contribution of the host galaxy, and a thermal component in the infrared band (Sun and Malkan 1988; Elvis et al. 1994). The line components have the same ratios as those derived in Francis et al. (1991), but the line intensities vary. The Ly α equivalent (and other lines accordingly) is scaled by factors between 0.5 and 5.0 from their nominal values in the composite quasar spectrum (Francis et al. 1991). The H α intensity is derived from the H β value, scaled up by a factor of three.

3.2. Color Separation

Running photometric-redshift tasks with two sets of templates of galaxies and power-laws, we test the results with objects with known spectroscopic redshifts. While HyperZ can pickup the majority of Type-I objects by the lower χ^2 values in the fitting output, it identifies $\sim 20\%$ of them as galaxies. Future work of improving the power-law templates and/or selective choice of galaxy templates may be needed. However, this uncertainty may be alleviated using the additional information in the X-ray bands. As discussed in Szokoly et al. (2004), the X-ray properties are indicative of object types. We pre-divide our sample into three groups based on their X-ray properties:

- Type-I AGN: $X_S - X_H > 0.1$ or and $X_H - R < 12$. Power-law templates;

- Type-II AGN: $X_S - X_H < 0.1$. Galaxy templates;
- Galaxies: $X_S - X_H > 0.1$ and $X_H - R > 12$. Galaxy templates.

The groups are established primarily by their X-ray hardness ratio and the X-ray-optical flux ratio, not on the broadband optical and infrared data. As shown in Figure 3B and 3D, nearly all Type-II AGN have X-ray magnitude difference $X_S - X_H > 0.1$. This parameter can also be interpreted as the hardness ratio $(H-S)/(H+S) > -0.2$, where H and S are the counts in the hard (2-10 keV) and soft (0.5-2 keV) bands, respectively. In addition, most galaxies are weaker emitter in the hard X-ray band, at $X_H - R > 12$, where R is the optical R-band magnitude. Once the initial separations are made, we manually check the broadband color of each object.

These selections are applied before our photometric-redshift estimations. The estimations for Type-II AGN and galaxies are made using the templates in HyperZ and BPZ, as their continuum features are primarily thermal. For Type-I AGN, we use our power-law templates and the HyperZ task, which allows a large number of templates. To check whether the results is overly dominated by one single band, we also run the datasets with and without the bluest band. This is one of the criteria used in the final determination of redshifts.

The source classification in Table 1 represents our best results: For the 137 objects where reliable redshifts are established, we use their broad-line properties to classify them. For the others, we use the COMBO-17 results. If sources are not in the COMBO-17 catalog, we use their X-ray properties to classify them. In a few cases when we have reasons to believe as exceptions, we discuss them in §4.3.

4. DISCUSSIONS

There are several sources of uncertainties and discrepancies in our redshift estimations: (1) Source confusion: Deep optical images often reveal multiple sources within the X-ray positional error circle. Many factors, such as the X-ray brightness and optical morphology, need to be considered before a careful decision may be made. (2) Complicated source energy distributions: Some X-ray sources have hybrid continuum shape, as the combination of a thermal component and a power law. Our model templates may not be sophisticated enough to reach the best and unique fits; and (3) Faintness of some sources: When the magnitudes are close to the detection limit, the task do poorly in distinguishing the Balmer and Lyman breaks.

4.1. Photo-z Confidence Levels

The results are cross-compared between HyperZ and BPZ. Our main concern is potential catastrophic errors between redshift ~ 0.5 and that of ~ 2.5 , which arise from the confusion between the Balmer continuum break and Lyman- α break. In such cases, the X-ray properties provide additional discriminators for the estimates of redshift. As shown in Figure 4, approximately 90% of the redshift values derived from BPZ and HyperZ match well. Their photometric redshifts and errors are calculated as the weighted average of BPZ and HyperZ. The weights are taken as the reciprocal of redshift errors, averaged over the lower and higher sides. Both BPZ and HyperZ output the confidence levels of photometric redshifts, which we use to calculate the errors in redshift. The new 95% confidence level of photometric redshift is calculated from the weighted average of errors, respectively, on the lower and higher redshift side. With such a method, the redshift values with narrower redshift range are given with more weights. Several pairs of seemingly discrepant redshifts are compromised as they converge towards the values with narrower redshift ranges. Several COMBO-17 redshifts do not have published error values (Wolf et al. 2004). We use the errors in the pairing BPZ or HPZ redshifts. Discrepant redshifts in approximately 15 sources are likely the results from (1) faint sources for which the uncertainties rise; and (2) some sources with power-law continua, for which the HyperZ evaluation is more reliable because of the added AGN templates. Nearly all the hard X-ray sources as well as the objects with large R-K colors are at lower redshifts ($z < 1.5$). Figure 5 compares photometric and spectroscopic redshifts. The average dispersion $\Delta z/(1 + z)$ is 0.08. We run a similar test for BPZ and HyperZ values. The dispersion is 0.08 for HyperZ values, and 0.10 for BPZ.

We assign quality indices to every source, from 0 to 3. With quality index 3, the spectroscopic redshift is certain, and so is the optical counterpart. It corresponds to quality index 2+ and higher in Szokoly et al. (2004). Index 2 means a secure spectroscopic redshift, but the optical counterpart is uncertain. Other index values are assigned with multiple factors, such as the COMBO-17 (0.4), BPZ (0.3), HyperZ (0.2), and single-line redshifts (1.0). The index values of 1 or smaller can be additive, e.g. if we have a single-line spectroscopic redshift, for which all three photo-z results agree, $Q=1.9$. The grading in photo-z does not mean to indicate a quality flag between BPZ and HyperZ.

Our main results are presented in Table 1. Three objects are marked with quality index of 0.2. In two such cases, a power-law continuum is apparent, and their fitting results with HyperZ must be specially chosen. In another case, the HyperZ values are supported by the X-ray spectroscopy. Two objects are marked with quality index of 0.3. It is very faint and are detected only in a few bands, leading to confusion between Ly α and Balmer breaks. In such cases, the BPZ values are chosen. Based on the redshift information, we are able to

fine tune the classification in §3.2 and further divide the three groups into seven:

- Galaxy: $L_x < 10^{42}$ ergs s $^{-1}$ with hardness ratio $HR < -0.2$.
- Type-2 AGN: $10^{42} < L_x < 10^{44}$ ergs s $^{-1}$ and the hardness ratio $HR > -0.2$.
- Type-2 QSO: $L_x > 10^{44}$ ergs s $^{-1}$ and the hardness ratio $HR > -0.2$.
- Type-1 AGN: $10^{42} < L_x < 10^{44}$ ergs s $^{-1}$ and the hardness ratio $HR < -0.2$.
- Type-1 QSO: $L_x > 10^{44}$ ergs s $^{-1}$ and the hardness ratio $HR < -0.2$.
- M-star

Figure 6 displays a comparison between the COMBO-17 results and our photometric redshifts for sources which do not have reliable spectroscopic redshifts. The latter are derived from the combination of BPZ and HyperZ, as described above. The redshift dispersion between these two samples is approximately 12%.

4.2. Comments on Individual Objects

The high quality of the *HST* images enables us to resolve many X-ray sources. We find that approximately forty sources show significant sub-arcsecond structure, *i.e.* two or more components with flux contrast less than 10. They are marked in Table 1 (in column "Offset"). Separation beyond that would have been identified in the EIS data. Three such sources show considerable color difference between bands, therefore implying discrepant redshifts.

Several sources show sub-arcsecond components of different colors. The source numbers refer to that in Giacconi et al. (2002), representing a unique detection number for each source. The optical cutout images for four such sources are displayed in Figure 7.

CDFS 27: This source consists of three components. Component A exhibits a similar magnitude to the other two, but it is significantly fainter in other bands.

CDFS 55: As shown in Figure 7, this source consists three distinct components in the V and B band separated by $\sim 0.^{\prime\prime}25$, and is extended in all four ACS bands. The component A is significant fainter in the B band, therefore implying a possibly different redshift.

CDFS 94: Three components within the X-ray error range. They can be seen marginally in Figure 13 of Giacconi et al. (2002).

CDFS 630: Multiple sub-arcsecond structure are shown at the bottom of Figure 7. Component B is brighter in the Z band.

The properties of a number of peculiar sources also need some discussions: are discussed in Mainieri et al. (2004). Here we discuss several other sources:

CDFS 38 and 100: The broad-band data of these two objects exhibit a power-law continuum without signs of emission lines. The spectrum of source 100 shows a single emission line around 8600Å, which may be O [II] 3737 at redshift 1.309.

CDFS 6 and 626: The data resemble a power-law continuum without a significant break. The HyperZ values may be more accurate. Alternative values of redshifts, based on galaxy models, are given near the end of Table 1.

CDFS 217, 243 and 508: Their primary BPZ values are at $z > 7$, but the X-ray spectroscopy reveals some features, which resemble iron K α lines. If we take the HyperZ values or the secondary BPZ values, the redshifts are between 2.5 and 4.6, are consistent with the X-ray results. More details will be discussed in (Mainieri et al. 2004).

CDFS 523: This source was within 2" from the list of red objects by Koekemoer et al. (2004). Since no confirmed detection is given in any optical or infrared bands, the counterpart may be another one which lies 1.9" and is weakly detected in several HST/ACS bands (AB ~ 27.4).

Table 2 lists four sources that are weakly detected only in one band (FORS-*R*, Giacconi et al. 2002), but not confirmed in the EIS multi-band images:

CDFS 261: *R*–band magnitude > 26.1 . No *HST* data are available.

CDFS 616: *R*–band magnitude > 26.1 . No *HST* data are available.

CDFS 640: *R*–band magnitude > 25.7 . No *HST* data are available.

CDFS 649: *R*–band magnitude > 25.7 . But the source detection is not confirmed by the *HST* data. The nearest counterpart in the *HST* data is 14" away.

No redshift information can be derived from these single-band detections. Furthermore, these sources are among the faintest in both the X-ray and optical bands. It is therefore possible that their detections may not be highly reliable.

4.3. Effect of Filter Bands and Sensitivity

Approximately 95% of the X-ray sources have infrared data. To test their effect on photometric redshifts, we run the tasks with only the optical bands. The average accuracy in redshift is reduced from $\sim 8\%$ to $\sim 12\%$. But the effect is redshift dependent: The most sensitive redshift ranges are between $0.8 < z < 2.5$, where the accuracy is at a level of 20%. This region is known for the lack of prominent spectral features in the optical bands. At other redshifts, the impact of infrared data is not so significant.

Our photometric redshifts also depend on the faintness of sources. If we establish a subgroup whose R-band magnitudes are within 1.5 magnitudes to the detection limit, the number of outliers increase significantly. This dependence on sensitivity may be from the same reason as stated above: Near the detection limit, the tasks may not distinguish Balmer breaks from Ly α breaks.

As discussed in §4.1, the dispersion of HyperZ results, as compared with spectroscopic redshifts, is slightly smaller than that for BPZ. This may be understood as our HyperZ fitting includes a large grid of simulated AGN-1 spectra, while the BPZ fitting uses only its built-in galaxy templates. Most spectroscopic redshifts are obtained for relatively bright sources, which include a large portion of Type-I AGN and QSOs. For fainter sources, we believe that BPZ has advantages as it takes the priors into consideration.

4.4. Evolution of X-Ray Properties

Figure 8 displays the redshift distribution of X-ray source numbers for the three groups defined in §3.2. Type-II AGN are mostly populated at $z < 1.5$, and galaxies at $z < 1$. Type-I AGN exhibit less redshift dependence. We also observe a significant peak in the redshift distribution at $z \sim 0.6$, which confirms a report (Tozzi et al. 2001; Szokoly et al. 2004) on the large-scale structure at several redshift positions.

Figure 9 displays the redshift dependence of X-ray luminosity. The X-ray luminosity is calculated with parameter $H_0 = 71 \text{ km s}^{-1} \text{ Mpc}^{-1}$, $\Omega_m = 0.3$ and $\Omega_\Lambda = 0.7$. The intrinsic luminosity of galaxies forms a low-end envelope. The hard-X-ray luminosities of Type-II AGN are comparable to that of Type-I AGN, but different in the optical. This may be in agreement with the assumption that they are intrinsically similar, but viewed at different angles. At edge-on positions, the optical and soft-X-ray flux may be subject to significant obscuration.

Our results are consistent with that derived from the spectroscopic redshifts (Fig. 22,

Szokoly et al. 2004), offering encouraging evidence that, with careful calibration, photometric redshifts are a reliable resource for the statistical study of distant sources. The redshift values in this paper have found their application in a recent study of the X-ray luminosity function (Norman et al. 2004).

4.5. Redshift Dependence of Color

As shown in Figure 10, there is significant evolution with redshift of X-ray and optical/near-IR colors. The hardness ratio declines with redshift. This is consistent with the finding of Gilli et al. (2003a) that most hard X-ray sources are at redshift lower than 1.5. While it is possible that a part of the observed trend may be the result of increasing luminosity threshold with redshift, the effect may not account for all the changes, as they are found in sources whose fluxes are well above the detection thresholds. At higher redshifts, a part of the hard X-ray flux is shifted into the soft X-ray band, thus reducing the hardness ratio. This effect may also explain the change in the U-K color: At higher redshifts, the K-band data represent only the data at the restframe wavelength $2.2/(1+z)$ μm , since the reddening effect becomes significantly lessened.

The change in the U-K color is mainly due to a simple redshift effect: At higher redshifts, the K-band data represent only the data at the restframe wavelength $2.2/(1+z)$ μm , since the reddening effect becomes significantly lessened.

As discussed by Szokoly et al. (2004), different types of X-ray sources are separated in the plot of X-ray hardness ratio vs. X-ray luminosity. Figure 11 demonstrates the same trend, with a significantly higher number of sources. We plot the relationship for both the hard- and soft-X-ray luminosities. Many galaxies are not detected in the hard X-ray band.

5. SUMMARY

We utilize a photometric redshift estimation using 12-band data in near-UV, optical, infrared and X-ray. We employ a set of power-law models for Type-I AGN and various models of galaxies, to derive the photometric redshifts for 342 CDFS sources. A comparison with the spectroscopic redshift of 137 objects suggests an average accuracy of approximately 8%. Our results well match that of COMBO-17. These encouraging results suggest that photometric redshifts are of significant accuracy.

The redshifts of CDFS sources subtend a broad range between 0.01 to 4.66. The hard X-ray sources, mostly Type-II AGN, are mainly populated at $z < 1.5$. The sources with

power-law continuum, *i.e.* Type-I AGN, show less redshift dependence.

Observations have been carried out using the ESO New Technology Telescope (NTT) and the 2.2m telescope at the La Silla observatory under Program-ID Nos. 61.A-9005(A), 162.O-0917, 163.O-0740, and 164.O-0561. This work has benefited from the GOODS project, which provides high quality VLT and *HST* images and source catalogs for a significant portion of the CDFS field. The HST data presented in this paper were obtained from MAST. STScI is operated by the Association of Universities for Research in Astronomy, Inc., under NASA contract NAS5-26555. Support for MAST for non-HST data is provided by the NASA Office of Space Science via grant NAG5-7584 and by other grants and contracts.

This work has been supported in part by NASA grant NAG-8-1527 and NAG-8-1133. W.Z. thanks Roser Pelló and Narciso Benítez for their kind help and advice on photometric redshift estimations.

REFERENCES

Arnouts, S., et al. 2001, A&A, 379, 740

Barger, A. J., et al. 2003, AJ, 126, 632

Beckwith, S. V. W., et al. 2003, BAAS, 35, 723

Benítez, N. 2000, ApJ, 536, 571

Bertin, E., and Arnouts, S. 1996, A&AS, 117, 393

Bolzonella, M., Miralles, J.-M., and Pelló, R. 2000, A&A, 363, 476

Bruzual, A., G., and Charlot, S. 1993, ApJ, 405, 538

Budavári, T., et al. 2001, AJ, 122, 1163

Coleman, G. D., Wu, C.-C., and Weedman, D. W. 1980, ApJS, 43, 393

Connolly, A. J., Szalay, A. S., Dickinson, M., Subbarao, M. U., Brunner, R. J. 1997, ApJ, 486, L11

Dickinson, M., et al. 2003, in “The Mass of Galaxies at Low and High Redshift”, eds. R. Bender and A. Renzini (New York: Springer), 324

Elvis, M., et al. 1994, ApJS, 95, 1

Francis, P. J., Hewett, P. C., Foltz, C. B., Chaffee, F. H., and Weymann, R.J. 1991, ApJ, 373, 465

Gandhi, P., Crawford, C. S., Fabian, A. C., and Johnstone, R. M. 2004, MNRAS, 348, 529

Giacconi, R., et al. 2000, ApJ, 551, 624

_____ 2002, ApJS, 139, 369

Giavalisco, M., et al. 2004, ApJ, 600, L93

Gilli, R., et al. 2003a, ApJ, 592, 721

Gilli, R. 2003b, astro-ph/0303115

Gonzalez, A. H., and Maccarone, T. J. 2002, ApJ, 581, 155

Hasinger, G., Burg, R., Giacconi, R., Schmidt, M., Trumper, J., and Zamorani, G. 1998, *A&A*, 329, 482

Koekemoer, A. M., 2004, *ApJ*, 600, L123

Koo, D. C. 1985, *AJ*, 90, 418

Lehmann, I., et al. 2001, *A&A*, 371, 833

Mainieri, V., et al. 2004, *A&A*, submitted

Mobasher, B., et al. 2004, *ApJ*, 600, L167

Norman, C., et al. 2004, *ApJ*, 607, 721

Renzini, A., et al. 2003, In *The Mass of Galaxies at Low and High Redshift*, eds. R. Bender and A. Renzini (New York: Springer), 332

Richards, G., et al., 2001, *AJ*, 122, 1151

Rosati, P., et al. 2002, *ApJ*, 566, 667

Sun, W., and Malkan, M. 1988, *ApJ*, 346, 68

Szokoly, G. P., et al. 2004, *ApJ*, submitted (astro-ph/0312324)

Tozzi, P., et al. 2001, *ApJ*, 562, 42

Vanden Berk, D., et al. 2001, *AJ*, 122, 549

Wolf, C., Dye, S., Kleinheinrich, M., Meisenheimer, K., Rix, H.-W., and Wisotzki, L. 2001a, *A&A*, 377, 442

Wolf, C., Meisenheimer, K., and Röser, H.-J. 2001b, *A&A*, 365, 660

Wolf, C., Meisenheimer, K., Rix, H.-W., Borch, A., Dye, S. and Kleinheinrich, M. 2003, *A&A*, 401, 73

Wolf, C., et al. 2004, *A&A*, in press, (astro-ph/0403666)

Figure Captions

Fig. 1.— Position offsets between the X-ray and Optical/Infrared data. Some sources are not detected in the EIS survey, and supplementary data are collected from the *HST* imaging data.

Fig. 2.— Multiband color of selected CDFS sources in restframe. The dotted lines represent Type-I quasars; dashed lines - Type-II quasars; and solid lines - galaxies. A composite SDSS spectrum of quasars (Vanden Berk et al. 2001) and a power-law template (without Ly α forest absorption) are plotted for comparison.

Fig. 3.— Properties of CDFS sources with known spectral type and redshift: (A) X-ray-to-optical ratio vs. redshift; (B) Hardness ratio vs. redshift; (C) X-ray-to-optical ratio vs. optical/infrared color; and (D) Hardness ratio vs. optical/infrared color. The open circles represent Type-I AGN; open squares Type-I quasars; filled circles Type-II AGN; filled squares Type-II quasars; triangles galaxies, and asterisks clusters.

Fig. 4.— Comparison of photometric redshifts of BPZ and HyperZ. The symbols are the same as Figure 3. Objects fainter than $R < 25$ are marked with smaller symbols. Stars represent the cases where broad-band SED resemble a power law. In most of these cases, spectroscopy or COMBO-17 data confirm the HyperZ values derived from power-law templates.

Fig. 5.— Comparison of photometric redshifts with spectroscopic redshift. The photometric redshifts are derived from Hyper-Z and BPZ. The symbols are the same as Figure 3. The object marked with an arrow consists of components of significantly different color (CDFS 55).

Fig. 6.— Comparison of photometric redshifts with COMBO-17 results. The photometric redshifts are derived from Hyper-Z and BPZ. The selection criteria are: (1) COMBO-17 magnitude is brighter than 24 in the R band; and (2) Spectroscopic redshift is unknown. The symbols are the same as Figure 3.

Fig. 7.— ACS cutout images of four sources with sub-arcsecond components. Their CDFS source identification numbers are marked at upper-left corner of each image, and the optical band name at the lower-right corner. The circles represent the 3σ X-ray positional errors, along with intensity contours. The dimension for each cutout is 3'', and the orientation follows that of the relevant ACS images, not aligned with the east-north direction. See discussion in §4.2.

Fig. 8.— Redshift distribution of X-ray sources. The shaded histograms show that for the

sources with spectroscopic redshifts. Galaxies are detected up to $z \sim 2$. They do not show an excess at $z \sim 0.7$.

Fig. 9.— X-ray luminosity vs. redshifts. The symbols are the same as in Figure 4. The curve represents the boundary for limiting flux. The symbols are the same as Figure 3.

Fig. 10.— Redshift dependence of optical-infrared color and X-ray hardness. The symbols are the same as Figure 3.

Fig. 11.— X-ray hardness vs. X-ray luminosity. The symbols are the same as Figure 3.

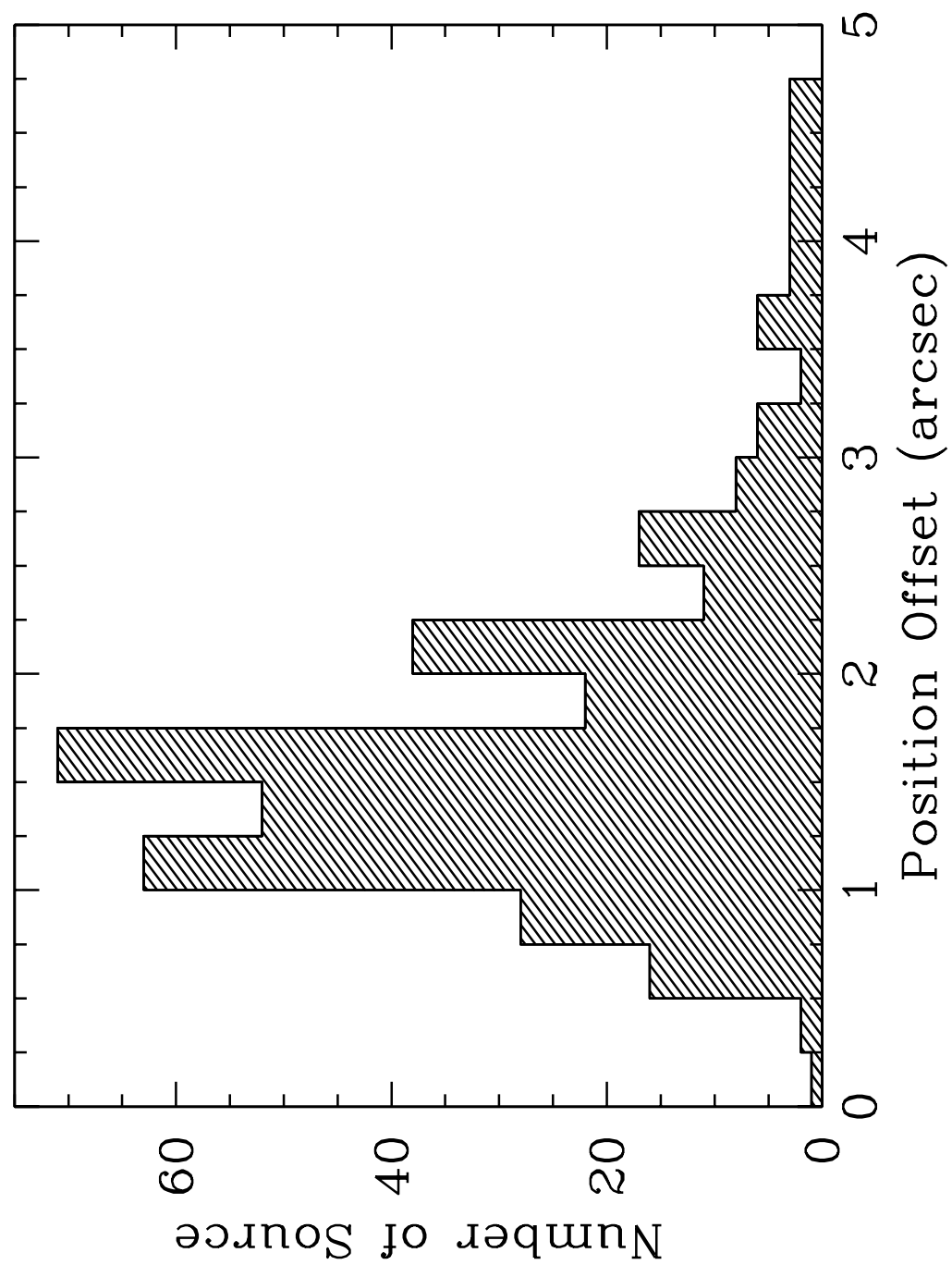


Fig. 1.—

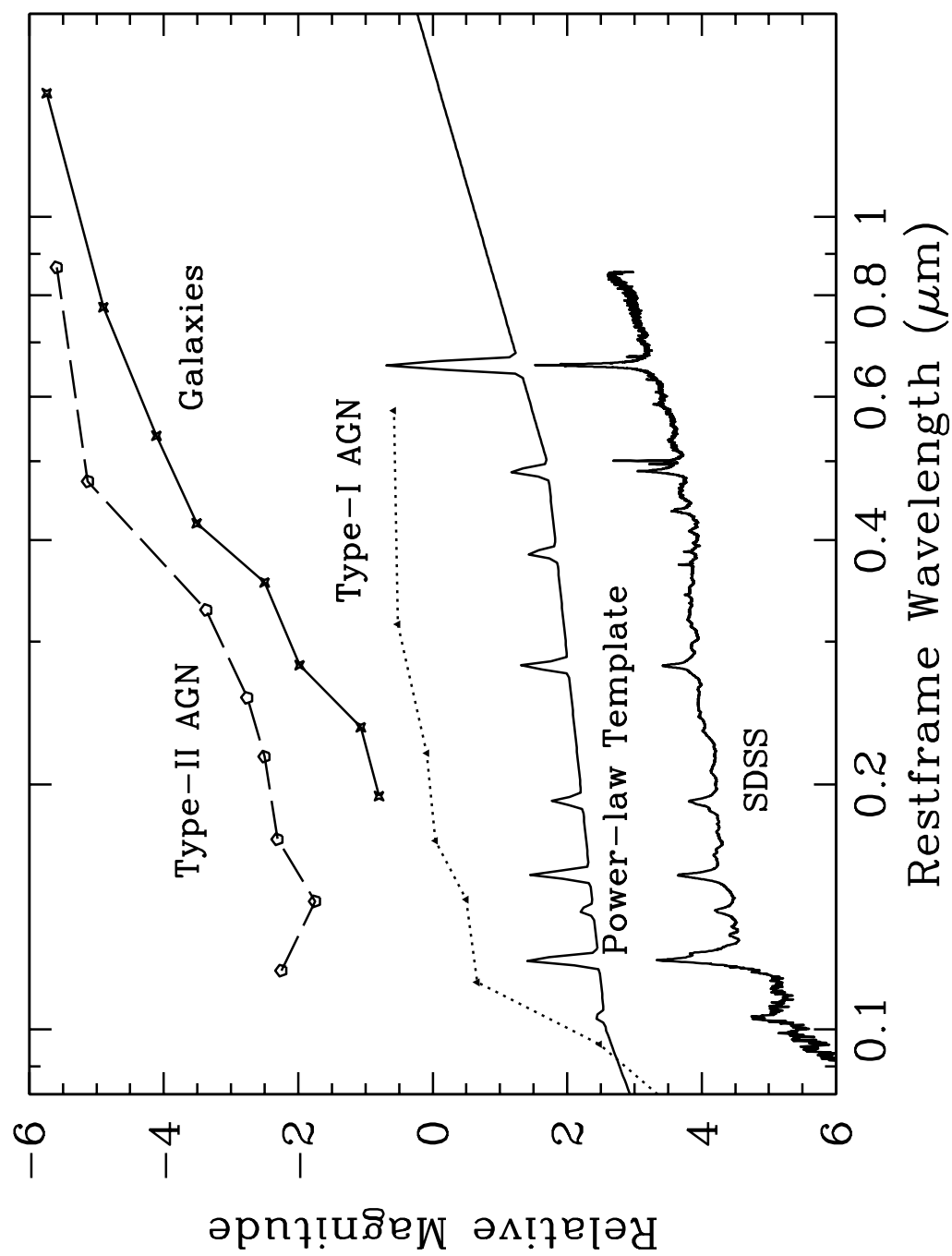


Fig. 2.—

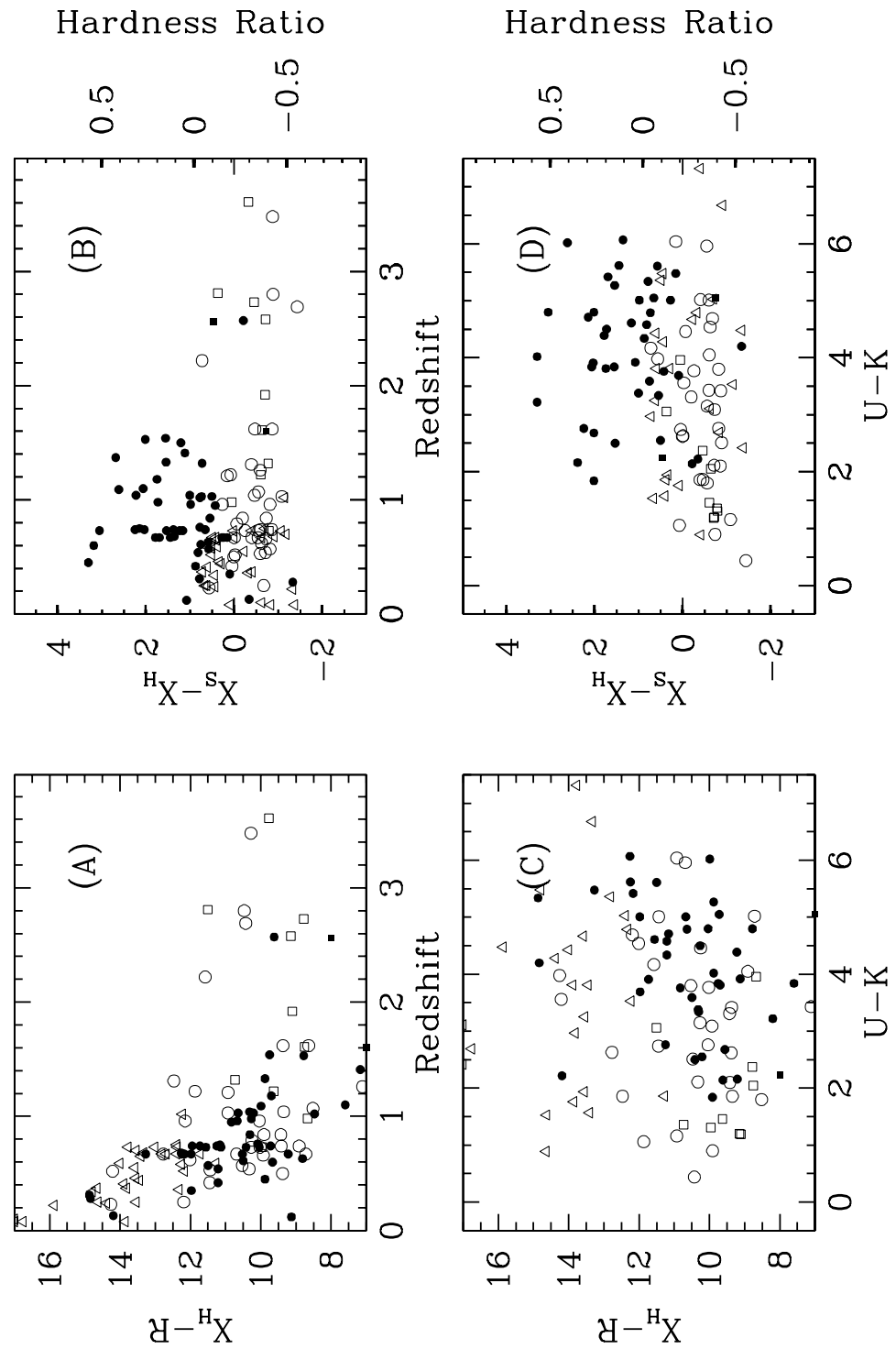


Fig. 3.—

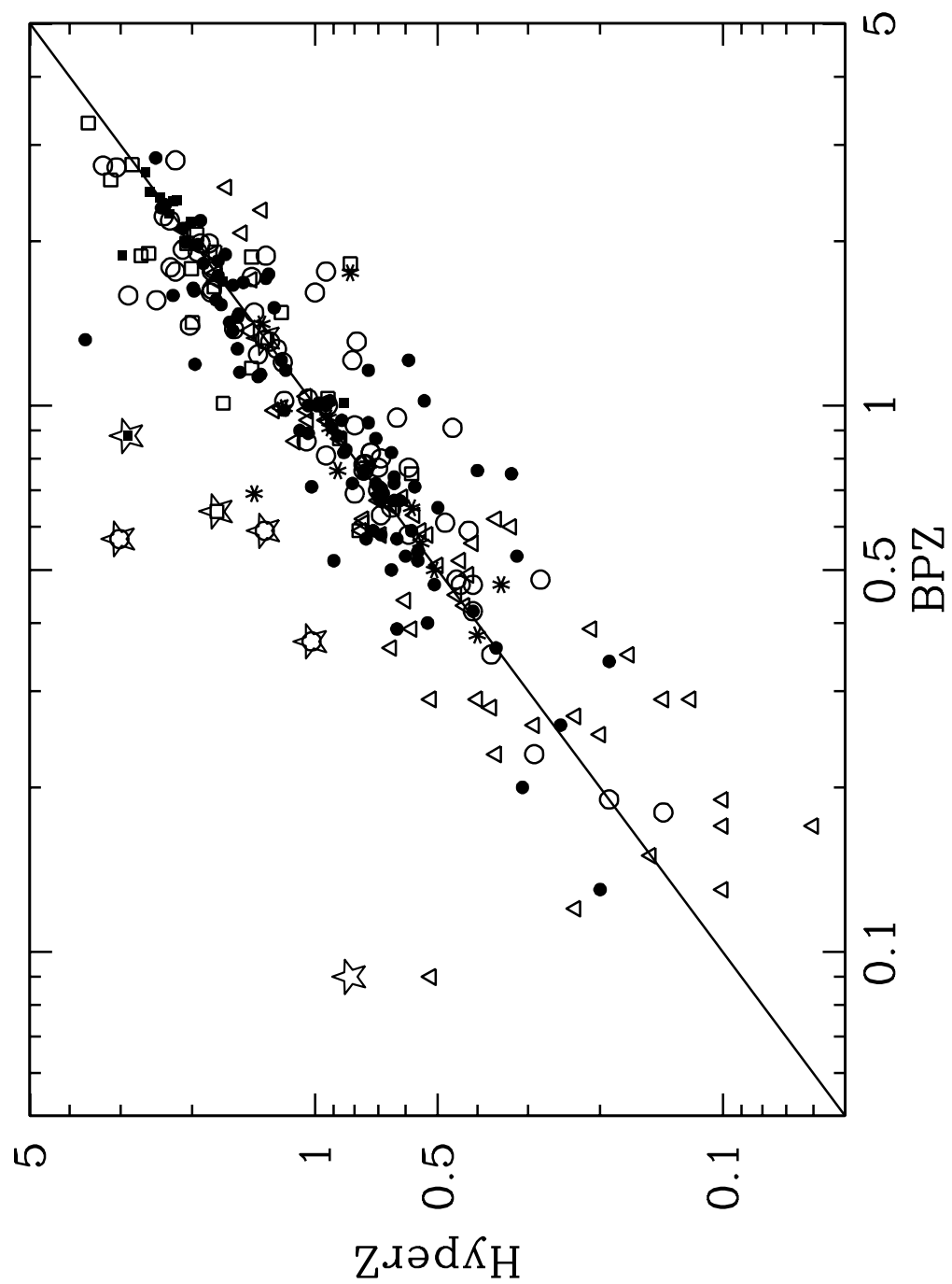


Fig. 4.—

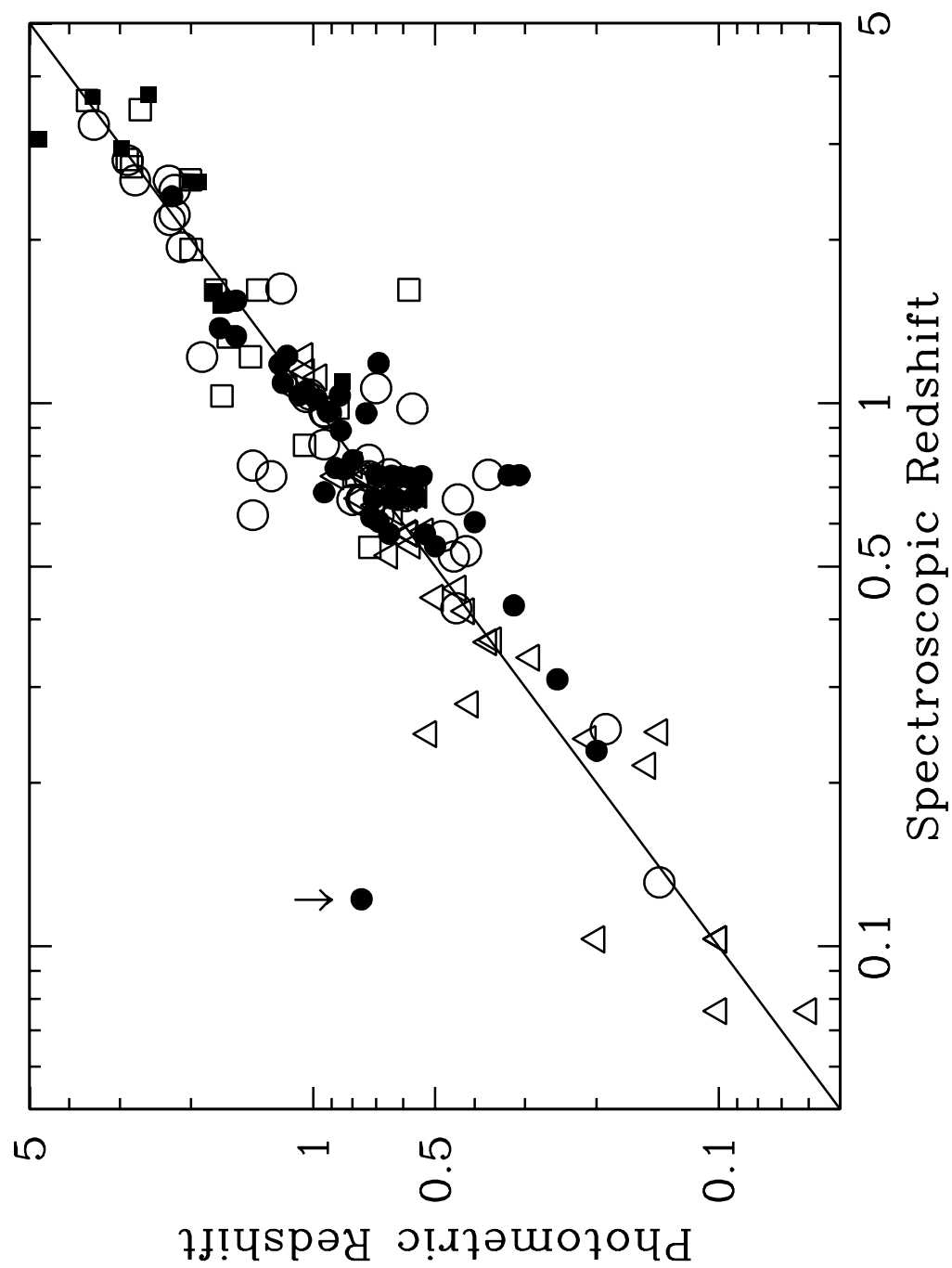


Fig. 5.—

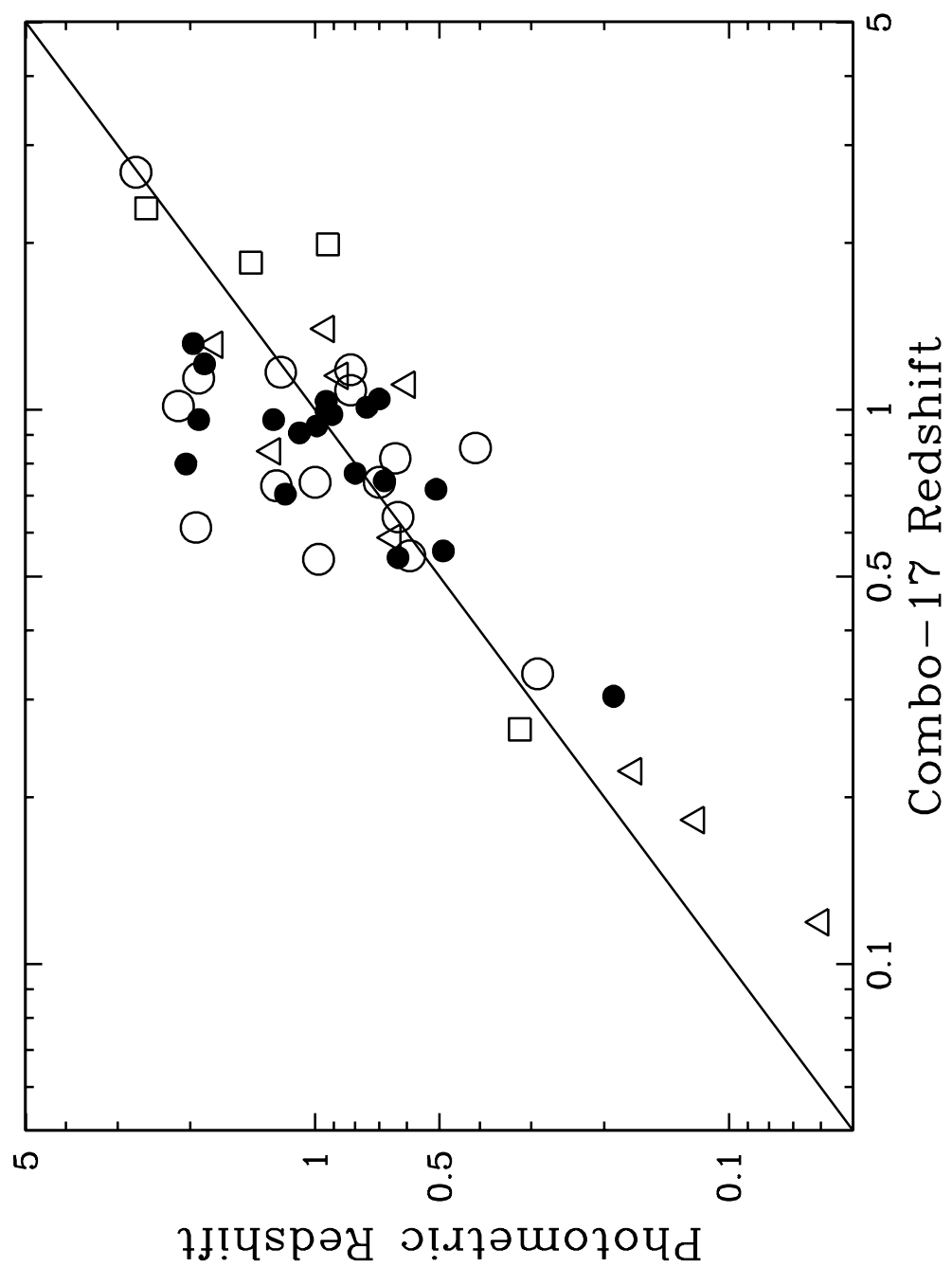


Fig. 6.—

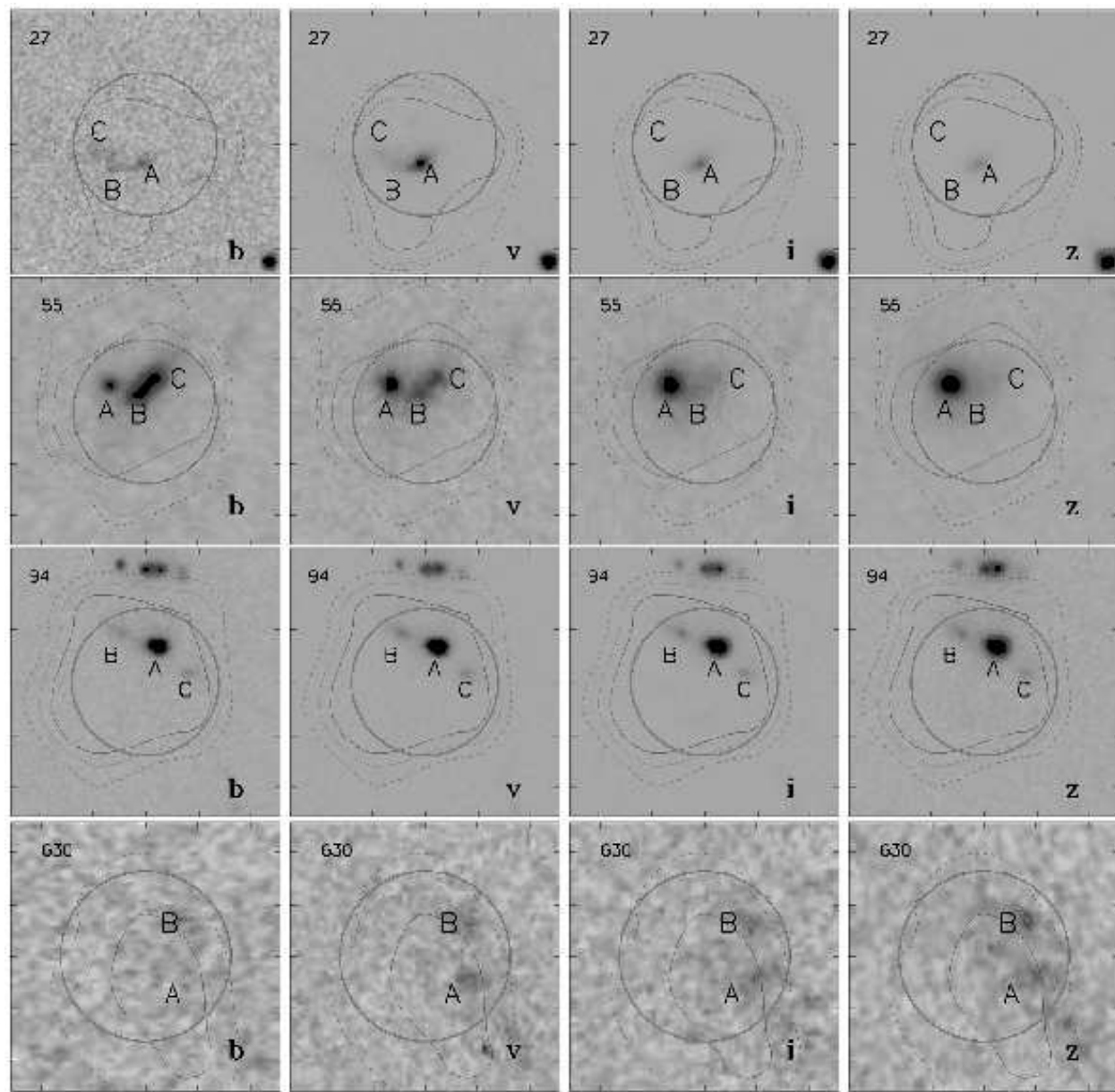


Fig. 7.—

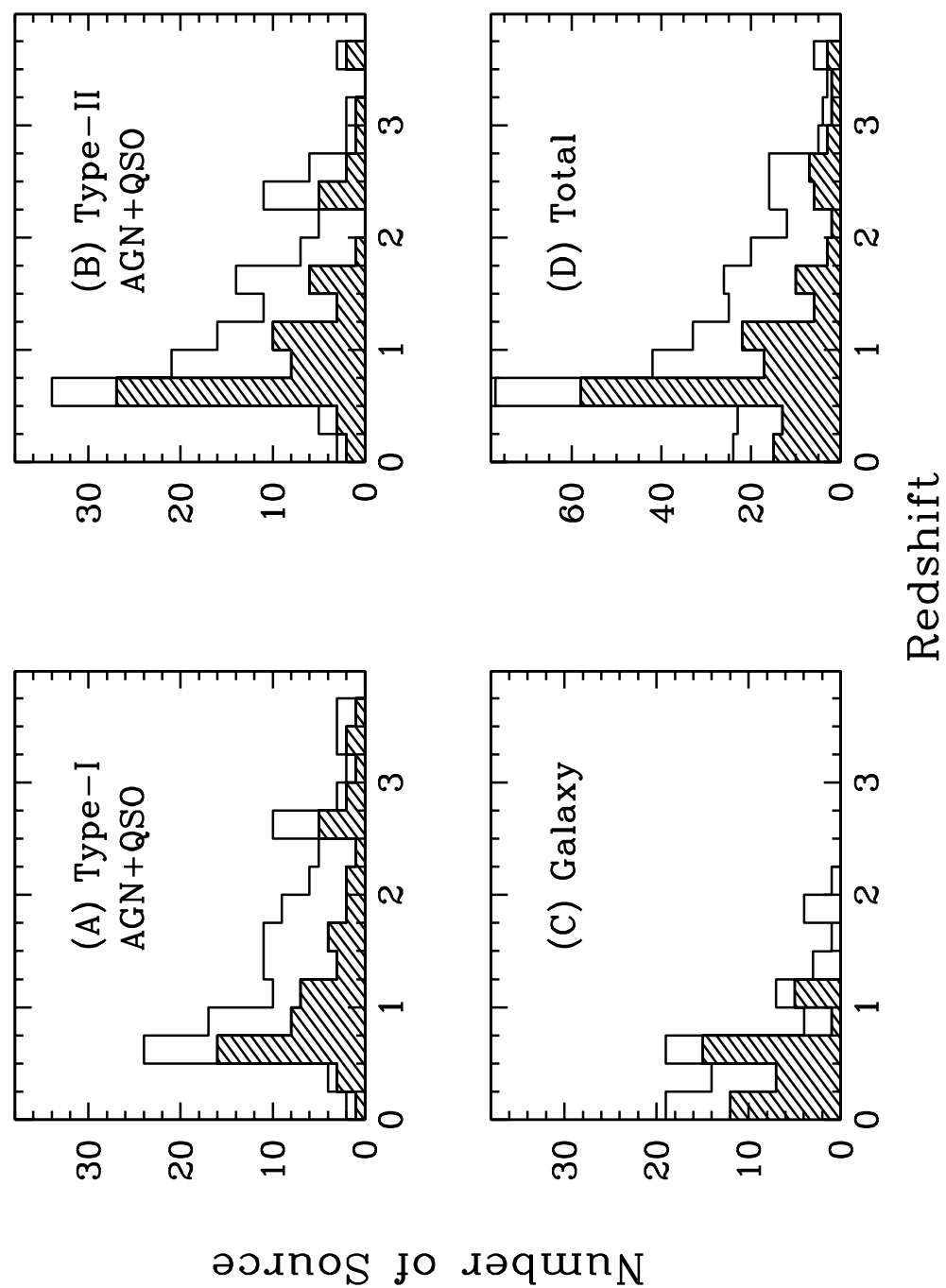


Fig. 8.—

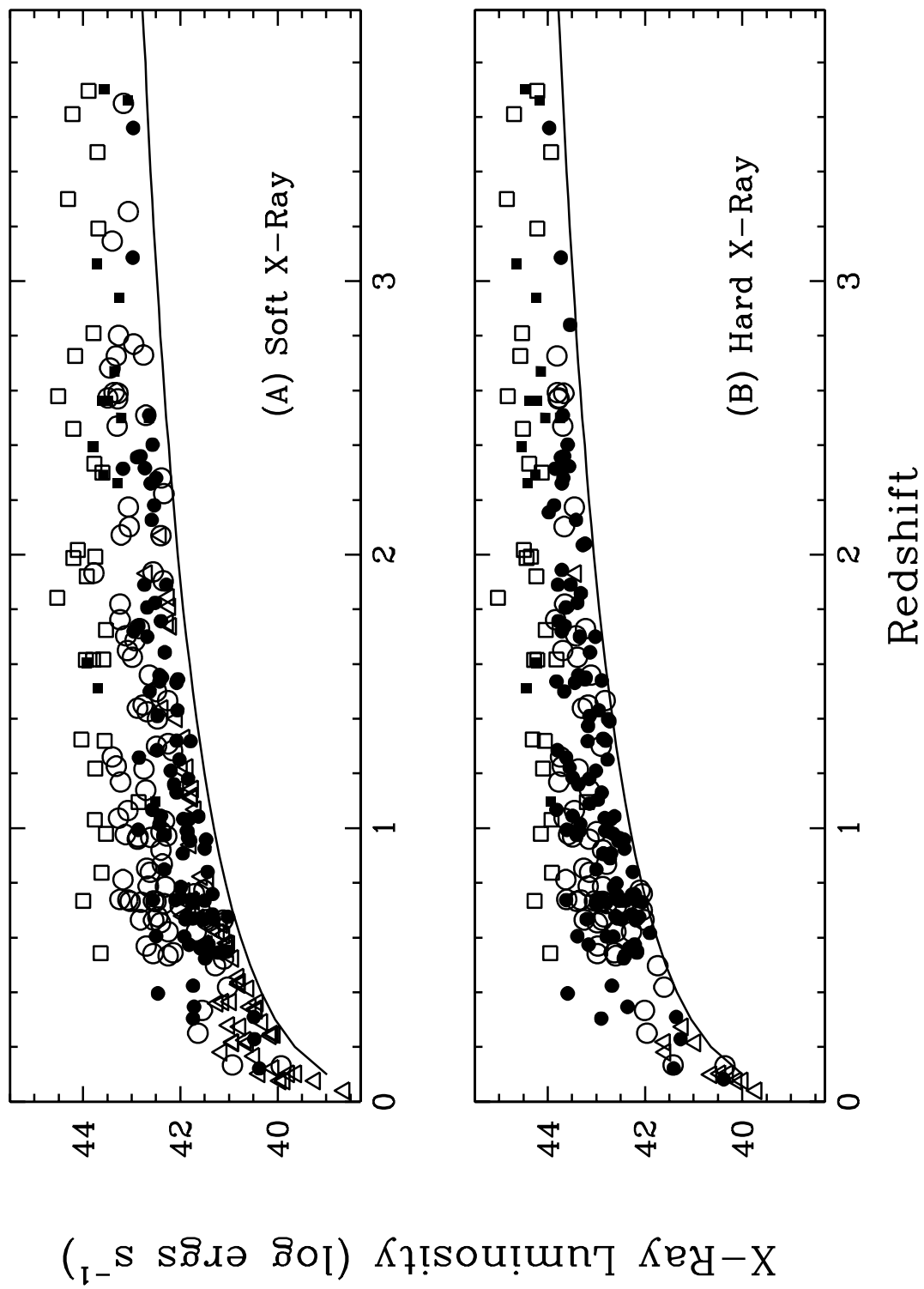


Fig. 9.—

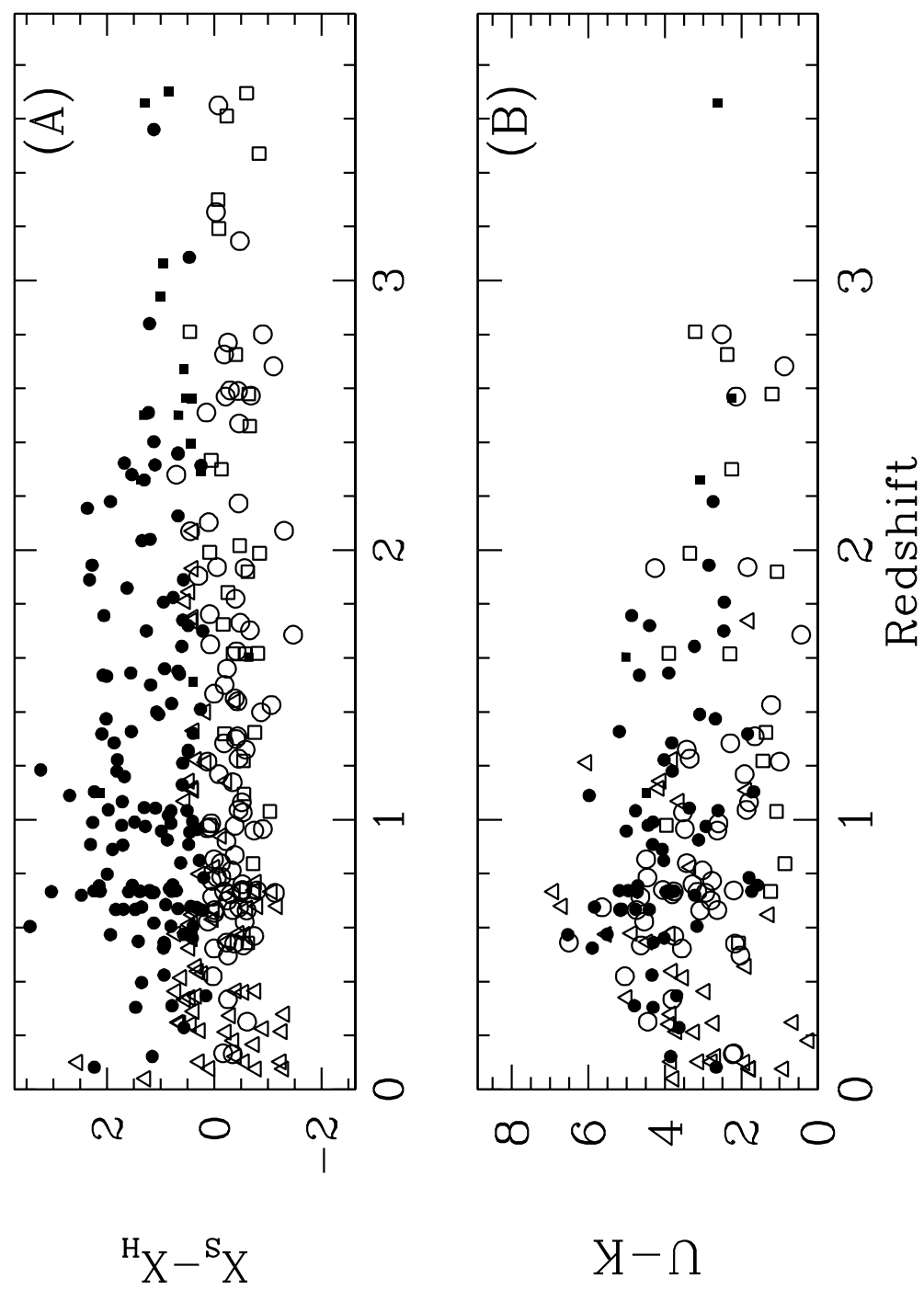


Fig. 10.—

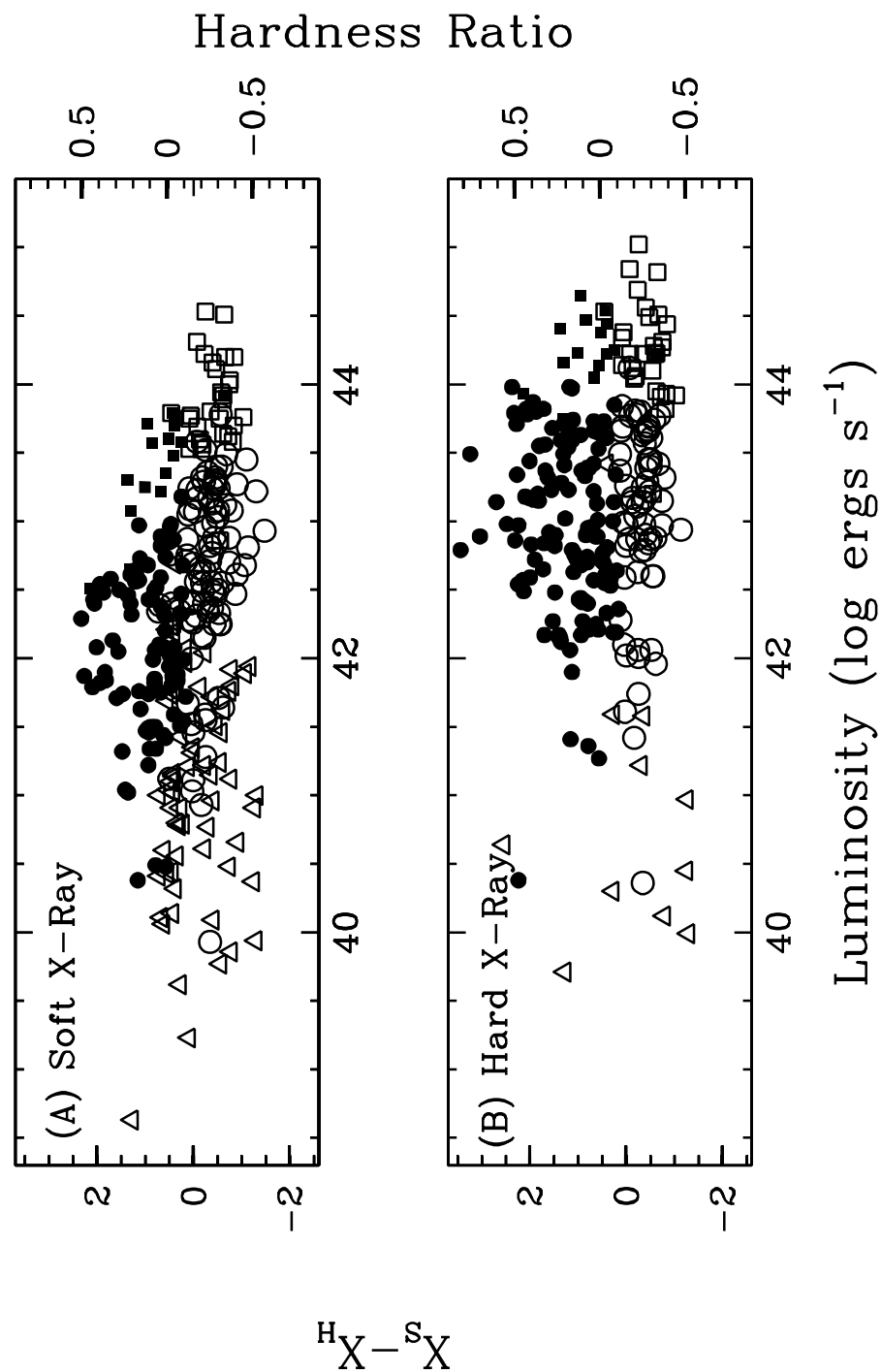


Fig. 11.—

Table 1. Photometric Redshifts of X-Ray Sources in Chandra Deep Field South

X-ray ID	α (2000) ^a	δ (J2000) ^a	Offset ('")	Redshift ^b	Range ^c	Type	Quality ^d
1	03 33 09.56	-27 46 03.9	0.9	0.35	...	AGN-2	1.6
2	03 33 08.78	-27 42 54.6	1.3	0.73	0.70 - 0.75	AGN-1	0.4
3	03 33 05.85	-27 46 53.6	3.1	0.22	0.12 - 0.32	Galaxy	0.4
4	03 33 03.53	-27 45 16.5	3.8	1.26	...	AGN-1	1.6
6	03 33 02.68	-27 48 23.4	0.8	2.46	2.39 - 2.50	QSO-1	0.2
7	03 33 01.71	-27 58 18.9	1.0	1.84	0.53 - 1.95	QSO-1	0.6 ^g
8	03 33 01.49	-27 41 42.4	0.8	0.99	0.92 - 1.03	AGN-2	0.9
9	03 33 00.76	-27 55 20.8	2.3	1.99	1.97 - 2.00	QSO-1	0.4
10	03 32 59.79	-27 46 26.6	1.6	0.42	...	AGN-2	3.0
11	03 32 59.85	-27 47 48.4	1.5	2.58	...	QSO-1	3.0
12	03 32 59.68	-27 50 30.6	1.8	0.25	...	AGN-1	3.0
13	03 32 59.07	-27 43 39.8	1.2	0.73	...	AGN-1	3.0
15	03 32 52.89	-27 51 20.1	1.5	1.23	...	AGN-1	1.5
17	03 32 49.11	-27 55 06.7	2.6 ^e	0.87	0.32 - 1.57	AGN-1	0.6
18	03 32 47.90	-27 42 33.1	1.2	0.98	...	QSO-1	3.0
19	03 32 47.92	-27 41 48.2	1.0	0.74	...	AGN-1	3.0
20	03 32 44.46	-27 49 40.5	1.3	1.02	...	AGN-2	3.0
21	03 32 44.32	-27 52 51.5	1.5	3.47	...	QSO-1	3.0
22	03 32 43.25	-27 49 14.4	1.2	1.92	...	QSO-1	3.0
23	03 32 41.72	-27 44 01.5	3.7	0.73	0.33 - 1.04	AGN-1	0.5
24	03 32 41.86	-27 52 02.7	1.6	3.61	...	QSO-1	3.0
25	03 32 40.64	-27 55 48.2	4.4	2.26	1.89 - 2.58	QSO-2	0.5
26	03 32 39.71	-27 46 11.3	1.5 ^e	1.65	1.36 - 1.89	AGN-1	0.5
27	03 32 39.59	-27 48 51.9	2.4 ^e	3.06	...	QSO-2	3.0
28	03 32 39.10	-27 46 02.0	1.0	1.22	...	AGN-1	3.0
29	03 32 38.95	-27 57 00.6	1.7	0.30	0.29 - 0.31	AGN-2	0.9
30	03 32 38.14	-27 39 45.0	1.4	0.84	...	QSO-1	3.0
31	03 32 37.78	-27 52 12.6	1.3 ^e	1.60	...	QSO-2	3.0
32	03 32 37.47	-27 40 00.3	1.0	0.66	...	AGN-1	3.0
33	03 32 36.73	-27 44 06.7	1.0	0.67	...	AGN-1	3.0
34	03 32 34.96	-27 55 11.2	1.8	0.84	...	AGN-1	3.0
35	03 32 34.44	-27 39 13.4	1.2	1.51	...	QSO-2	3.0
36	03 32 32.98	-27 45 45.9	2.9 ^e	0.33	0.32 - 0.35	AGN-1	0.9
37	03 32 32.11	-27 41 55.4	1.7 ^e	0.99	0.62 - 1.06	AGN-1	0.9
38	03 32 30.23	-27 45 04.8	1.2	0.74	...	AGN-1	3.0
39	03 32 29.99	-27 45 30.1	1.2	1.22	...	QSO-1	3.0
40	03 32 29.01	-27 57 30.5	1.5	0.55	0.50 - 0.58	AGN-1	0.9

Table 1—Continued

X-ray ID	α (2000) ^a	δ (J2000) ^a	Offset (")	Redshift ^b	Range ^c	Type	Quality ^d
41	03 32 27.64	-27 41 45.1	0.9	0.67	...	AGN-2	3.0
42	03 32 27.02	-27 41 05.2	0.9	0.73	...	QSO-1	3.0
43	03 32 26.78	-27 41 45.8	1.6	0.74	...	AGN-2	3.0
44	03 32 26.51	-27 40 35.8	1.0	1.03	...	QSO-1	3.0
45	03 32 25.71	-27 43 05.8	0.8	2.29	2.14 - 2.60	QSO-2	1.5
46	03 32 25.17	-27 42 19.0	1.4	1.62	...	QSO-1	3.0
47	03 32 24.99	-27 41 01.8	1.4	0.73	...	AGN-2	3.0
48	03 32 24.87	-27 56 00.1	1.7 ^e	1.26	1.03 - 1.49	AGN-2	0.5
49	03 32 24.26	-27 41 26.7	1.1	0.53	...	AGN-1	3.0
50	03 32 19.03	-27 47 55.4	1.1	0.67	...	AGN-2	1.9
51	03 32 17.19	-27 52 20.8	1.6 ^e	1.10	...	QSO-2	3.0
52	03 32 17.15	-27 43 03.5	1.2	0.57	...	AGN-1	3.0
53	03 32 14.99	-27 51 27.1	1.7	0.68	...	AGN-1	3.0
54	03 32 14.60	-27 54 20.9	2.3	2.56	...	QSO-2	3.0
55	03 32 14.02	-27 51 00.9	1.4 ^e	0.12	...	AGN-2	3.0
56	03 32 13.26	-27 42 41.1	0.7	0.60	...	AGN-2	3.0
57	03 32 12.96	-27 52 37.0	1.6	2.56	...	QSO-2	3.0
58	03 32 11.80	-27 46 28.4	1.0	0.92	0.58 - 1.22	AGN-1	0.5
59	03 32 11.37	-27 52 13.9	1.9	0.97	0.32 - 4.11	AGN-1	0.5
60	03 32 10.93	-27 44 15.1	1.0	1.61	...	QSO-1	3.0
61	03 32 10.36	-27 43 11.3	3.5	2.02	1.72 - 2.32	QSO-1	0.5
62	03 32 09.47	-27 48 06.9	1.2	2.81	...	QSO-1	3.0
63	03 32 08.68	-27 47 34.5	1.2	0.54	...	QSO-1	3.0
64	03 32 07.88	-27 46 58.5	3.0	0.13	0.11 - 0.16	AGN-1	0.4
65	03 32 03.90	-27 53 29.2	1.5	1.10	1.08 - 1.12	QSO-1	0.5
66	03 32 03.67	-27 46 03.8	1.1	0.57	...	AGN-2	3.0
67	03 32 02.47	-27 46 00.5	0.9	1.62	...	QSO-1	3.0
68	03 32 01.60	-27 43 27.2	0.6	2.73	...	QSO-1	3.0
69	03 32 01.47	-27 41 38.9	0.5	0.85	0.57 - 1.14	AGN-1	0.4
70	03 32 01.23	-27 46 47.3	3.8	1.07	0.88 - 1.15	AGN-2	0.4
71	03 32 00.37	-27 43 19.9	1.1	1.04	...	AGN-1	3.0
72	03 31 58.29	-27 50 42.0	1.4	1.99	1.76 - 2.21	QSO-1	0.5
73	03 31 58.12	-27 48 34.2	1.0	0.73	...	AGN-1	3.0
74	03 31 57.80	-27 42 08.9	0.8	0.65	0.59 - 0.72	AGN-1	0.9
75	03 31 55.39	-27 54 48.3	0.8	0.74	...	AGN-2	3.0
76	03 31 52.53	-27 50 17.6	0.8	2.39	...	QSO-2	1.2
77	03 33 01.53	-27 45 42.7	2.2	0.62	...	AGN-1	3.0

Table 1—Continued

X-ray ID	α (2000) ^a	δ (J2000) ^a	Offset (")	Redshift ^b	Range ^c	Type	Quality ^d
78	03 32 30.07	-27 45 23.7	1.3 ^e	0.96	...	AGN-1	3.0
79	03 32 38.05	-27 46 26.7	0.9	1.91	1.77 - 1.97	AGN-1	0.5
80	03 32 10.94	-27 48 57.5	1.6	1.70	1.42 - 2.04	AGN-1	0.5
81	03 32 25.97	-27 45 14.6	1.2	2.59	2.35 - 2.60	AGN-1	0.5
82	03 32 15.09	-27 51 04.8	2.2	1.89	1.69 - 2.05	AGN-2	0.5
83	03 32 14.99	-27 42 25.2	0.5 ^e	1.76	1.68 - 1.85	AGN-1	0.5
84	03 32 46.77	-27 42 12.2	1.7	0.10	...	Galaxy	3.0
85	03 32 44.62	-27 48 36.2	1.0 ^e	2.59	...	AGN-1	1.2
86	03 32 33.86	-27 45 20.6	1.1	3.09	2.96 - 3.36	AGN-2	0.5
87	03 32 18.25	-27 52 41.5	1.6	2.80	...	AGN-1	3.0
89	03 32 08.28	-27 41 53.8	0.5	2.47	...	AGN-1	3.0
90	03 32 42.01	-27 57 02.9	2.0	Star	3.0
91	03 32 42.85	-27 47 02.7	1.0 ^e	3.19	...	QSO-1	1.0
92	03 32 49.66	-27 54 54.1	2.1	Star	3.0
93	03 32 02.34	-27 52 34.0	1.5	1.30	1.06 - 2.05	AGN-1	0.5
94	03 32 44.02	-27 46 34.9	1.9 ^e	1.69	1.56 - 1.89	AGN-1	0.5
95	03 32 29.89	-27 44 24.4	0.8	0.08	...	Galaxy	3.0
96	03 32 20.93	-27 52 22.8	1.2	0.27	0.15 - 0.73	Galaxy	0.6
97	03 32 11.10	-27 40 56.0	1.7	0.18	...	Galaxy	2.0
98	03 32 44.28	-27 51 41.4	1.0	0.28	...	Galaxy	3.0
99	03 32 05.27	-27 53 57.9	1.7	0.79	0.56 - 0.90	AGN-1	0.5
100	03 32 36.00	-27 48 50.6	0.9	1.31	...	AGN-1	1.9
101	03 32 55.50	-27 47 53.5	1.9 ^e	1.62	...	AGN-1	3.0
103	03 32 28.83	-27 43 55.8	1.2	0.21	...	Galaxy	3.0
108	03 32 05.72	-27 44 48.4	2.2	1.56	1.40 - 1.76	AGN-1	0.5
110	03 32 58.61	-27 46 32.2	2.0	0.62	...	AGN-1	3.0
112	03 31 51.96	-27 53 27.3	1.8	2.94	...	QSO-2	3.0
114	03 32 07.63	-27 52 13.8	1.4	1.72	1.55 - 1.92	AGN-2	0.5
116	03 32 30.00	-27 44 04.9	1.2	0.08	...	Galaxy	3.0
117	03 32 03.06	-27 44 50.3	1.0	2.57	...	AGN-1	3.0
121	03 31 51.17	-27 50 51.8	1.8	0.67	...	AGN-2	3.0
122	03 32 57.58	-27 45 48.8	1.8	2.10	1.63 - 2.46	AGN-1	0.5
124	03 32 02.45	-27 45 25.6	3.0	0.61	0.29 - 0.93	Galaxy	0.5
132	03 32 44.02	-27 54 54.4	2.0 ^e	0.91	...	AGN-2	1.4
133	03 32 02.79	-27 44 28.8	3.5	1.21	0.35 - 6.95	AGN-2	0.5
138	03 32 50.02	-27 41 36.0	1.5	0.97	...	AGN-1	3.0
145	03 32 22.55	-27 46 04.1	1.3	1.50	1.37 - 1.69	AGN-2	0.5

Table 1—Continued

X-ray ID	α (2000) ^a	δ (J2000) ^a	Offset (")	Redshift ^b	Range ^c	Type	Quality ^d
146	03 32 47.05	-27 53 33.4	2.4	2.67	2.47 - 2.85	QSO-2	0.5
147	03 32 46.36	-27 46 32.4	1.0	0.99	0.79 - 1.21	AGN-2	0.5
148	03 32 35.21	-27 53 18.0	1.8	1.74	1.50 - 2.02	AGN-2	0.5
149	03 32 12.24	-27 46 20.8	1.3 ^e	1.03	...	AGN-2	3.0
150	03 32 25.17	-27 54 50.2	1.7	1.09	...	AGN-2	3.0
151	03 32 20.49	-27 47 32.5	1.3	0.60	...	AGN-2	3.0
152	03 32 59.33	-27 48 59.1	1.5	1.28	1.20 - 2.26	AGN-2	0.6
153	03 32 18.35	-27 50 55.1	1.7	1.54	...	AGN-2	3.0
155	03 32 07.99	-27 42 39.5	0.9	0.55	...	AGN-2	3.0
156	03 32 13.23	-27 55 28.8	1.4	1.19	...	AGN-2	3.0
159	03 32 50.25	-27 52 51.9	2.0 ^e	3.30	3.04 - 3.62	QSO-1	0.5
170	03 32 46.41	-27 54 14.2	1.6	0.66	...	AGN-2	3.0
171	03 32 35.10	-27 44 11.1	1.4	1.64	1.37 - 1.91	AGN-2	0.5
173	03 32 16.75	-27 43 27.7	1.3	0.52	...	Galaxy	3.0
174	03 33 01.20	-27 44 20.9	0.9	1.55	1.45 - 1.61	AGN-2	0.5
175	03 32 51.83	-27 44 37.0	1.8	0.52	...	AGN-1	3.0
176	03 33 09.24	-27 44 50.0	1.7	0.79	...	AGN-1	3.0
177	03 32 56.96	-27 50 08.9	1.5	1.14	...	Galaxy	3.0
178	03 32 13.89	-27 50 33.5	1.3	0.29	0.17 - 6.79	Galaxy	0.5
179	03 31 49.51	-27 50 34.2	1.3	2.73	2.56 - 2.90	AGN-1	0.5
183	03 32 34.19	-27 56 44.8	3.6	0.08	0.01 - 0.21	AGN-2	0.5
184	03 32 48.19	-27 52 56.9	1.7	0.67	...	AGN-2	3.0
185	03 32 10.93	-27 43 43.2	1.5	0.93	0.83 - 1.05	AGN-2	0.9
186	03 32 52.36	-27 45 56.8	1.2 ^e	1.11	0.92 - 1.30	Galaxy	0.4
188	03 32 22.56	-27 49 49.9	1.2	0.73	...	AGN-2	3.0
189	03 32 45.75	-27 42 13.0	2.1	0.76	...	AGN-2	3.0
190	03 32 35.86	-27 40 59.7	2.2	0.73	...	AGN-2	3.0
200	03 32 54.97	-27 45 07.1	0.9	0.85	0.75 - 1.38	AGN-2	0.4
201	03 32 39.06	-27 44 39.3	1.4	0.68	...	AGN-2	3.0
202	03 32 29.87	-27 51 06.0	1.3	3.70	...	QSO-2	3.0
203	03 32 26.69	-27 40 13.6	0.6 ^e	1.17	0.92 - 1.50	AGN-1	0.7
204	03 32 23.17	-27 45 54.9	0.9	1.22	...	Galaxy	3.0
205	03 32 17.11	-27 41 37.2	1.3	1.56	1.31 - 2.30	AGN-2	0.5
206	03 32 16.21	-27 39 30.5	1.2	1.32	...	QSO-1	3.0
207	03 32 07.91	-27 37 33.4	2.8	0.40	0.30 - 0.50	AGN-2	0.4
208	03 31 52.54	-27 46 42.5	0.9	0.72	0.63 - 0.81	AGN-1	0.6
209	03 31 47.29	-27 53 13.8	1.3	1.32	1.07 - 1.73	QSO-1	0.5

Table 1—Continued

X-ray ID	α (2000) ^a	δ (J2000) ^a	Offset (")	Redshift ^b	Range ^c	Type	Quality ^d
210	03 32 38.33	-27 55 53.3	1.8	1.73	1.47 - 2.17	AGN-1	0.5
211	03 32 05.92	-27 54 49.7	1.7	0.68	...	Galaxy	3.0
213	03 32 00.45	-27 53 56.1	2.8	0.60	0.19 - 1.73	AGN-2	0.5
217	03 32 33.03	-27 52 02.9	4.4	3.65	3.21 - 4.38	AGN-1	0.2 ^h
218	03 32 16.37	-27 52 01.3	2.3 ^e	0.50	...	AGN-1	1.4
219	03 31 50.42	-27 51 52.1	1.7	1.73	1.55 - 1.92	QSO-1	0.5
220	03 32 32.76	-27 51 51.3	1.4	1.40	1.37 - 1.42	AGN-1	0.5
221	03 32 08.83	-27 44 23.8	2.5	2.51	2.17 - 2.73	AGN-1	0.5
222	03 32 54.53	-27 45 02.1	0.8	1.14	0.88 - 1.40	AGN-1	0.4
224	03 32 28.77	-27 46 20.7	0.8	0.74	...	Galaxy	3.0
225	03 31 49.42	-27 46 34.4	1.3	2.30	2.27 - 2.33	QSO-1	0.6
226	03 32 04.42	-27 46 43.2	2.0	1.45	0.83 - 2.29	AGN-1	0.5
227	03 32 05.47	-27 46 46.8	2.2	2.18	1.78 - 2.54	AGN-2	0.5
229	03 32 56.34	-27 48 34.1	2.1	0.10	...	Galaxy	3.0
230	03 31 53.55	-27 48 43.1	1.4	2.17	...	AGN-1	3.0
232	03 31 55.84	-27 49 21.4	1.3	0.94	0.69 - 1.20	Galaxy	0.6
233	03 32 25.76	-27 49 36.4	1.7	0.58	...	Galaxy	3.0
236	03 32 11.46	-27 50 06.7	1.1	0.76	0.70 - 1.26	AGN-1	0.6
237	03 32 58.52	-27 50 08.1	1.5	Star	3.0
238	03 31 47.98	-27 50 45.4	1.5	1.06	...	AGN-1	3.0
239	03 32 36.18	-27 51 26.8	1.4	1.47	1.22 - 1.72	AGN-1	0.5
240	03 32 58.96	-27 51 41.8	3.8 ^e	1.41	1.29 - 1.65	AGN-2	0.5
241	03 32 24.22	-27 42 58.0	1.1	0.70	0.64 - 0.87	AGN-1	0.5
242	03 32 51.86	-27 42 29.7	1.1	1.03	...	AGN-1	3.0
243	03 32 08.41	-27 40 47.1	1.3	2.50	1.50 - 3.50	QSO-2	0.3 ⁱ
244	03 32 04.33	-27 40 26.7	1.1	0.97	0.31 - 3.95	AGN-1	0.5
246	03 32 22.86	-27 39 36.9	1.3	0.71	0.64 - 0.79	AGN-1	0.5
247	03 32 35.09	-27 55 33.2	3.2	0.04	...	Galaxy	3.0
248	03 32 10.24	-27 54 16.4	2.1	0.69	...	AGN-2	3.0
249	03 32 19.29	-27 54 06.2	3.0	0.96	...	AGN-2	2.0
251	03 32 07.27	-27 52 29.2	1.1	2.13	2.03 - 2.29	AGN-2	0.5
252	03 32 47.05	-27 43 46.6	0.7 ^e	1.18	...	AGN-2	3.0
253	03 32 20.05	-27 44 47.7	1.3 ^e	1.89	...	AGN-2	1.9
254	03 32 19.88	-27 45 18.2	1.5 ^e	0.10	0.01 - 0.12	Galaxy	0.7
256	03 32 43.07	-27 48 45.1	1.0	1.53	1.47 - 1.58	AGN-2	0.5
257	03 32 13.39	-27 48 57.8	1.6	0.55	...	AGN-2	1.5
259	03 32 06.14	-27 49 27.8	1.4	1.76	1.63 - 1.88	AGN-2	0.5

Table 1—Continued

X-ray ID	α (2000) ^a	δ (J2000) ^a	Offset (")	Redshift ^b	Range ^c	Type	Quality ^d
260	03 32 25.12	-27 50 43.2	1.6	1.04	...	AGN-2	3.0
263	03 32 18.87	-27 51 34.4	2.4	3.66	...	QSO-2	3.0
264	03 32 29.76	-27 51 46.9	0.6	1.32	...	AGN-2	1.9
265	03 32 33.31	-27 42 36.4	1.2 ^e	1.16	1.02 - 1.32	AGN-2	0.5
266	03 32 13.85	-27 42 49.1	1.7	0.73	...	AGN-2	3.0
267	03 32 04.85	-27 41 27.5	1.7 ^e	0.72	...	AGN-2	1.2
268	03 32 49.22	-27 40 50.6	1.8	1.22	...	AGN-2	3.0
501	03 33 10.19	-27 48 42.2	2.0	0.81	0.75 - 0.87	AGN-1	0.6
502	03 33 08.17	-27 50 33.4	1.4	0.73	0.65 - 0.81	AGN-2	0.6
503	03 33 07.62	-27 51 27.2	1.9	0.54	0.34 - 0.74	AGN-1	0.4
504	03 33 05.67	-27 52 14.5	2.0	0.52	0.00 - 0.66	AGN-2	0.6
505	03 33 04.80	-27 47 31.9	2.5	2.26	2.06 - 2.44	AGN-2	0.5
506	03 33 03.04	-27 51 45.8	2.1	3.69	3.12 - 4.19	QSO-1	0.5
507	03 33 00.14	-27 49 23.4	2.1	0.99	0.88 - 1.00	AGN-2	0.6
508	03 32 51.66	-27 52 13.0	2.2	2.50	1.50 - 3.50	QSO-2	0.5
509	03 32 42.22	-27 57 51.6	3.4	0.56	0.46 - 0.60	AGN-2	0.6
510	03 32 38.79	-27 51 22.1	0.9 ^e	2.51	2.17 - 2.67	AGN-2	0.5
511	03 32 36.44	-27 46 31.6	2.9	0.77	...	AGN-1	2.0
512	03 32 34.36	-27 43 50.3	1.5	0.67	...	AGN-2	3.0
513	03 32 34.00	-27 48 59.7	1.3	3.52	3.26 - 3.80	AGN-2	0.5
514	03 32 33.47	-27 43 12.9	1.5	0.10	...	Galaxy	3.0
515	03 32 32.21	-27 46 51.7	0.8	2.19	2.15 - 2.45	AGN-2	0.5
516	03 32 31.37	-27 47 25.1	2.8	0.67	...	AGN-1	3.0
517	03 32 30.14	-28 00 24.4	2.5	2.33	0.00 - 2.88	QSO-1	0.6
518	03 32 26.78	-27 46 04.0	1.5	0.84	0.32 - 1.90	AGN-2	0.5
519	03 32 25.87	-27 55 06.5	2.4 ^e	1.03	...	AGN-2	3.0
520	03 32 25.94	-27 39 27.7	0.3 ^e	0.79	...	AGN-2	3.0
521	03 32 22.78	-27 52 24.0	1.4	0.13	...	AGN-1	3.0
522	03 32 21.42	-27 55 49.5	1.9 ^e	2.57	...	AGN-1	2.0
523	03 32 20.49	-27 42 27.2	1.9	1.32	0.32 - 8.5	AGN-2	0.3 ^j
524	03 32 19.95	-27 42 43.1	1.5 ^e	2.36	1.98 - 2.80	AGN-2	0.5
525	03 32 19.81	-27 41 22.9	1.3	0.23	...	AGN-2	3.0
526	03 32 18.71	-27 44 12.8	1.7 ^e	0.96	...	AGN-2	3.0
527	03 32 18.37	-27 54 12.1	4.0	4.49	3.41 - 5.14	AGN-1	0.5
528	03 32 17.14	-27 54 02.6	1.2 ^e	1.43	0.82 - 1.96	AGN-2	0.5
529	03 32 16.41	-27 55 24.4	2.0	0.73	0.58 - 0.89	AGN-2	0.6
530	03 32 14.91	-27 38 43.8	0.2	1.04	0.88 - 1.21	AGN-2	0.6

Table 1—Continued

X-ray ID	α (2000) ^a	δ (J2000) ^a	Offset (")	Redshift ^b	Range ^c	Type	Quality ^d
531	03 32 14.44	-27 51 10.9	1.4	1.54	...	AGN-2	3.0
532	03 32 14.08	-27 42 30.2	2.0 ^e	0.95	0.54 - 1.37	AGN-2	0.9
533	03 32 14.03	-27 56 01.6	1.1	0.54	0.43 - 0.77	AGN-2	0.5
534	03 32 12.21	-27 45 30.3	0.6	0.68	...	AGN-2	3.0
535	03 32 11.42	-27 46 50.2	1.1 ^e	0.57	...	AGN-2	3.0
536	03 32 10.77	-27 42 34.8	1.9 ^e	0.42	...	AGN-1	3.0
537	03 32 09.83	-27 50 14.1	2.6	1.54	1.08 - 1.72	AGN-2	0.5
538	03 32 08.54	-27 46 48.4	1.4	0.31	...	AGN-2	3.0
539	03 32 04.07	-27 37 25.7	0.6	0.98	...	AGN-1	3.0
540	03 32 02.57	-27 50 52.8	1.4	1.25	1.16 - 1.34	AGN-2	0.5
541	03 31 59.59	-27 49 47.8	2.7	1.82	1.13 - 2.68	AGN-2	0.5
542	03 31 58.43	-27 54 35.7	1.6	1.70	1.04 - 3.15	AGN-2	0.5
543	03 31 56.99	-27 51 00.6	1.5	1.81	1.64 - 1.90	AGN-2	0.5
544	03 31 54.48	-27 51 05.7	2.6	2.36	2.14 - 2.57	AGN-2	0.5
545	03 31 54.41	-27 41 59.0	1.5	0.97	0.93 - 2.47	AGN-2	0.6
546	03 31 52.33	-27 47 52.5	1.5	2.31	2.19 - 2.38	AGN-2	0.5
547	03 31 50.41	-27 52 37.9	2.4	2.32	...	AGN-2	1.2
548	03 31 44.88	-27 51 59.1	2.5	1.44	1.41 - 1.46	AGN-1	0.5
549	03 32 22.57	-27 58 05.7	2.1	Star	3.0
550	03 33 00.60	-27 57 47.6	3.4	1.93	1.81 - 2.06	AGN-1	0.5
551	03 32 16.15	-27 56 44.3	1.8	2.68	2.57 - 2.84	AGN-1	0.6
552	03 32 15.81	-27 53 24.8	1.3	0.67	...	Galaxy	3.0
553	03 32 56.66	-27 53 16.7	2.5	0.37	...	Galaxy	3.0
554	03 31 50.77	-27 53 01.1	1.5	0.23	0.05 - 3.13	Galaxy	0.6
555	03 32 37.97	-27 53 08.0	1.6	2.28	1.94 - 2.64	AGN-1	0.5
556	03 32 00.44	-27 52 28.8	0.8	0.63	...	Galaxy	3.0
557	03 32 37.99	-27 43 59.4	2.7	1.81	1.69 - 2.11	Galaxy	0.5
558	03 31 58.16	-27 44 59.6	0.8	0.57	...	Galaxy	3.0
559	03 32 57.13	-27 45 34.4	2.0	0.01	0.00 - 0.02	Galaxy	0.6
560	03 32 06.28	-27 45 36.9	1.1	0.67	...	Galaxy	3.0
561	03 32 22.44	-27 45 43.7	1.1 ^e	0.62	0.38 - 1.12	Galaxy	0.5
562	03 31 51.51	-27 45 54.1	0.6	0.36	0.06 - 1.15	Galaxy	0.5
563	03 32 31.47	-27 46 23.2	1.7 ^e	2.22	...	AGN-1	3.0
564	03 32 16.71	-27 46 38.1	1.5	0.43	0.03 - 0.65	Galaxy	0.5
565	03 32 24.87	-27 47 06.4	1.3	0.36	...	Galaxy	3.0
566	03 32 18.03	-27 47 18.7	1.4 ^e	0.73	...	Galaxy	2.0
567	03 32 38.80	-27 47 32.5	1.2	0.46	...	Galaxy	3.0

Table 1—Continued

X-ray ID	α (2000) ^a	δ (J2000) ^a	Offset (")	Redshift ^b	Range ^c	Type	Quality ^d
568	03 33 10.91	-27 47 36.6	4.0	3.15	2.78 - 3.37	AGN-1	0.5
569	03 31 48.06	-27 48 01.9	1.3	2.07	1.96 - 2.19	AGN-1	0.5
570	03 32 22.55	-27 48 04.5	1.5	1.28	1.04 - 1.76	AGN-1	0.5
571	03 33 03.77	-27 48 10.9	1.2	1.44	1.42 - 1.45	Galaxy	0.5
572	03 32 22.19	-27 48 11.4	1.2	2.73	1.69 - 2.63	AGN-1	0.5
573	03 32 44.45	-27 48 19.3	1.0	0.41	...	Galaxy	3.0
574	03 32 31.56	-27 48 53.8	1.9	1.84	1.65 - 2.05	Galaxy	0.5
575	03 32 17.08	-27 49 21.9	1.6	0.34	...	Galaxy	3.0
576	03 31 44.00	-27 49 28.3	4.4	1.50	1.37 - 1.66	AGN-1	0.5
577	03 32 36.19	-27 49 32.0	1.8 ^e	0.55	...	Galaxy	3.0
578	03 32 48.55	-27 49 34.9	0.7	1.12	...	Galaxy	3.0
579	03 32 34.06	-27 49 37.8	2.1 ^e	0.82	0.54 - 1.00	Galaxy	0.9
580	03 32 15.99	-27 49 43.4	2.7 ^e	0.66	...	AGN-1	3.0
581	03 32 07.37	-27 49 42.0	2.2 ^e	0.80	0.17 - 0.90	Galaxy	0.6
582	03 32 38.83	-27 49 56.5	1.0	0.24	...	Galaxy	3.0
583	03 32 13.86	-27 50 00.5	2.1	2.77	2.55 - 2.99	AGN-1	0.5
584	03 32 17.86	-27 50 07.0	1.4	Star	3.0
585	03 31 55.53	-27 50 29.7	2.9	1.21	...	Galaxy	1.6
586	03 32 39.48	-27 50 32.0	1.1	0.58	...	Galaxy	3.0
587	03 32 15.29	-27 50 39.4	2.1	0.25	...	Galaxy	3.0
588	03 31 55.62	-27 50 44.0	0.4	Star	3.0
589	03 32 25.83	-27 51 20.3	1.3	1.33	0.45 - 8.50	Galaxy	0.5
590	03 32 07.12	-27 51 28.7	2.4	0.35	0.05 - 1.08	Galaxy	0.5
591	03 31 44.75	-27 51 37.1	4.1	1.43	1.33 - 1.47	AGN-1	0.5
592	03 32 47.19	-27 51 47.8	1.3	1.07	...	Galaxy	3.0
593	03 32 14.79	-27 44 02.5	1.4	2.07	1.59 - 2.23	Galaxy	0.5
594	03 32 09.71	-27 42 48.4	2.2	0.73	...	Galaxy	2.0
595	03 32 15.77	-27 39 54.1	1.0	0.36	0.19 - 0.98	Galaxy	0.5
596	03 32 31.81	-27 57 14.3	1.7	1.94	1.84 - 1.99	AGN-2	0.5
597	03 32 51.35	-27 55 44.0	0.6	2.32	2.24 - 2.40	AGN-2	0.5
598	03 32 24.69	-27 54 11.6	1.7	0.62	...	AGN-2	3.0
599	03 32 29.80	-27 53 28.6	1.8	2.84	2.12 - 3.00	AGN-2	0.5
600	03 32 13.84	-27 45 25.9	0.9	1.33	...	AGN-2	3.0
601	03 32 18.46	-27 45 56.0	1.4	0.73	...	AGN-2	3.0
602	03 32 22.00	-27 46 56.1	1.2	0.67	...	AGN-2	3.0
603	03 32 57.69	-27 47 10.9	1.5	2.04	1.56 - 2.32	AGN-2	0.5
604	03 31 48.63	-27 47 14.9	0.7	2.15	1.61 - 2.48	AGN-2	0.5

Table 1—Continued

X-ray ID	α (2000) ^a	δ (J2000) ^a	Offset (")	Redshift ^b	Range ^c	Type	Quality ^d
605	03 32 39.17	-27 48 32.4	1.5	4.29	4.13 - 4.35	AGN-2	0.5
606	03 32 24.99	-27 50 08.0	1.3	1.04	...	AGN-2	1.9
607	03 31 59.55	-27 50 20.1	2.0	1.10	0.86 - 1.35	AGN-2	0.6
608	03 33 03.86	-27 50 26.3	1.7	0.89	...	AGN-2	3.0
609	03 32 36.19	-27 50 37.1	1.0	1.86	1.69 - 2.02	AGN-2	0.5
610	03 32 19.81	-27 52 02.9	3.7	2.04	1.84 - 2.30	AGN-2	0.5
611	03 32 41.56	-27 43 27.9	2.7 ^e	0.98	...	AGN-2	1.9
612	03 32 21.35	-27 42 29.3	2.7	0.74	...	AGN-2	3.0
613	03 32 24.56	-27 40 10.7	1.7	0.91	0.78 - 0.99	AGN-2	0.9
614	03 32 34.82	-27 40 42.1	2.6 ^e	1.13	0.07 - 2.01	AGN-2	0.5
615	03 32 01.30	-27 50 50.9	1.5	0.76	...	AGN-2	3.0
617	03 32 31.43	-27 57 26.4	1.6	0.58	0.51 - 0.64	Galaxy	0.6
618	03 32 29.30	-27 56 19.6	2.2	4.66	4.52 - 4.78	AGN-1	0.5
619	03 31 55.63	-27 54 02.4	1.1	1.94	...	AGN-1	3.0
620	03 32 30.18	-27 53 06.1	1.8 ^e	0.65	...	Galaxy	3.0
621	03 32 16.58	-27 52 45.7	2.0	0.33	0.13 - 0.70	Galaxy	0.5
622	03 32 50.00	-27 44 07.3	3.6	1.75	1.39 - 2.11	Galaxy	0.6
623	03 32 28.44	-27 47 00.4	1.9 ^e	1.74	1.55 - 1.94	Galaxy	0.5
624	03 32 29.22	-27 47 07.7	1.5	0.67	...	Galaxy	3.0
625	03 32 00.92	-27 47 56.9	2.1	1.14	1.05 - 1.24	Galaxy	0.6
626	03 32 09.47	-27 47 57.2	1.7	1.90	1.74 - 1.95	AGN-1	0.2 ^k
627	03 32 23.36	-27 48 52.6	2.5	0.25	...	Galaxy	3.0
628	03 32 55.20	-27 51 02.8	4.2	2.07	1.95 - 2.27	AGN-1	0.5
629	03 32 53.34	-27 51 04.9	2.1	0.56	0.42 - 0.66	Galaxy	0.5
630	03 32 28.29	-27 44 03.5	0.6	3.25	...	AGN-1	3.0
631	03 32 15.08	-27 43 35.5	1.7	1.40	0.76 - 1.55	Galaxy	0.9
632	03 32 33.72	-27 52 28.8	2.7	0.63	0.59 - 0.65	AGN-2	0.5
633	03 31 50.43	-27 52 12.3	1.7	1.37	...	AGN-2	3.0
634	03 32 51.46	-27 47 47.3	1.2	1.40	1.28 - 1.54	AGN-2	0.5
635	03 32 16.80	-27 50 07.9	2.8 ^e	0.73	...	AGN-2	2.0
636	03 31 50.24	-27 50 46.9	4.5	0.80	0.70 - 1.32	AGN-2	0.4
637	03 32 25.90	-27 43 34.1	2.9 ^e	0.76	0.65 - 0.99	AGN-2	0.5
638	03 32 29.95	-27 43 01.5	1.4 ^e	1.39	1.29 - 1.42	AGN-2	0.9
639	03 32 52.63	-27 42 39.3	1.4	0.99	0.87 - 1.12	AGN-2	0.6
641	03 32 39.17	-27 59 19.2	1.4	0.74	0.67 - 0.82	AGN-2	0.6
642	03 32 15.18	-27 41 59.0	2.6	2.40	...	AGN-2	3.0
643	03 31 56.33	-27 52 56.5	1.6	1.93	1.85 - 2.43	Galaxy	0.5

Table 1—Continued

X-ray ID	α (2000) ^a	δ (J2000) ^a	Offset (")	Redshift ^b	Range ^c	Type	Quality ^d
644	03 32 45.96	-27 57 45.6	1.2	0.12	0.10 - 0.15	Galaxy	0.6
645	03 31 49.85	-27 49 44.3	3.0	0.68	...	Galaxy	2.0
646	03 32 45.12	-27 47 24.3	1.5	0.44	...	Galaxy	3.0
647	03 33 01.83	-27 50 09.5	1.8	Star	3.0
648	03 32 46.54	-27 57 13.4	2.7	0.77	...	Galaxy	3.0
650	03 33 07.33	-27 44 32.9	0.9	0.21	0.17 - 0.26	Galaxy	0.6
651	03 32 28.42	-27 58 10.3	2.1	0.17	0.09 - 0.25	Galaxy	0.6
652	03 32 49.33	-27 43 02.4	1.1	0.08	...	Galaxy	3.0
653	03 33 03.72	-27 44 11.0	0.9	0.91	0.66 - 1.15	AGN-2	0.6

^aUnique CDFS identification number. See Table 2 of Giacconi et al. (2002)

^bOptical/infrared counterpart, in units of hr., min., sec., deg., min., and sec.

^cValues with no range are spectroscopic redshifts (except stars)

^dAt 95% confidence level

^e0.2: HyperZ only; 0.3: BPZ only; 0.4: COMBO-17 only; 0.5: BPZ and HyperZ; 0.6: COMBO-17 and HyperZ; 0.7: COMBO-17 and BPZ; 0.9: COMBO-17, BPZ and HyperZ; 1.2: Single-line spectrum and HyperZ; 1.6: Single-line spectrum, COMBO-17, and HyperZ; 1.9: Single-line spectrum, COMBO-17, BPZ and HyperZ ; 2.0: Secure spectroscopic redshift, but optical counterpart uncertain; 3.0: Secure spectroscopic redshift

^fMultiple sub-arcsecond structure in HST images

^gBased on power-law templates. BPZ value: $z = 1.33$ (1.02 – 2.54)

^hBased on HyperZ. BPZ yields $z > 7$

ⁱBased on the secondary value of BPZ. HyperZ: $z = 3.45$ (3.10 – 3.86)

^jBased on BPZ. HyperZ: $z = 3.66$ (2.95 – 5.12)

^kBased on power-law templates. BPZ value: $z = 0.59$ (0.51 – 0.65)

Table 2. CDFS Sources without Redshift

X-ray ID ^a	α (J2000) ^b	δ (J2000) ^b
261	03 31 57.11	-27 51 10.9
616	03 32 25.58	-27 58 43.2
640	03 32 17.74	-27 38 52.1
649	03 32 24.85	-27 38 51.5

^aUnique CDFS identification number

^b*Chandra* coordinates, in units of hr., min., sec., deg., min., and sec. From Giacconi et al. (2002)